Article

OSP-1 protects neurons from autophagic cell death induced by acute oxidative stress

Alessandra Donato[1], Fiona K. Ritchie [1], Lachlan Lu[1], Mehershad Wadia[1], Ramon Martinez-Marmol[1], Eva Kaulich [1], Kornraviya Sankorrakul[2], Hang Lu [3], Sean Coakley [2], Elizabeth J. Coulson [1,2] & Massimo A. Hilliard [1] ✉

Oxidative stress, caused by the accumulation of reactive oxygen species (ROS), is a pathological factor in several incurable neurodegenerative conditions as well as in stroke. However, our knowledge of the genetic elements that can be manipulated to protect neurons from oxidative stress-induced cell death is still very limited. Here, using *Caenorhabditis elegans* as a model system, combined with the optogenetic tool KillerRed to spatially and temporally control ROS generation, we identify a previously uncharacterized gene, *oxidative stress protective 1* (*osp-1*), that protects *C. elegans* neurons from oxidative damage. Using rodent and human cell cultures, we also show that the protective effect of OSP-1 extends to mammalian cells. Moreover, we demonstrate that OSP-1 functions in a strictly cell-autonomous fashion, and that it localizes to the endoplasmic reticulum (ER) where it has an ER-remodeling function. Finally, we present evidence suggesting that OSP-1 may exert its neuroprotective function by influencing autophagy. Our results point to a potential role of OSP-1 in modulating autophagy, and suggest that overactivation of this cellular process could contribute to neuronal death triggered by oxidative damage.

Reactive oxygen species (ROS) are by-products of cellular respiration and the primary cause of oxidative stress. At physiological levels, ROS regulate a variety of signaling pathways, including those involved in metabolism and stress resistance[1,2]. However, when their concentration increases due to overproduction or insufficient degradation, ROS can cause oxidative damage to DNA, RNA, proteins, and lipids[3,4]. The brain is particularly susceptible to oxidative damage[5], with this chemical insult being implicated in a variety of neurodegenerative disorders, including Parkinson's, Alzheimer's, and Huntington's diseases[6–14], as well as in stroke[15–17]. One of the cellular events that are triggered by oxidative stress is autophagy[1,2,18–21], a mechanism of cellular degradation with important homeostatic functions[22]. In this context, autophagy has been shown to reduce ROS-induced stress by degrading oxidized proteins and damaged organelles[22]. However, whether neuronal autophagy has a protective role or represents a degenerative modality is still under debate.

Genetically tractable animal model systems, such as the nematode *Caenorhabditis elegans* (*C. elegans*), in which ROS production can be directly induced in the nervous system, can facilitate a better understanding of the cellular mechanisms activated by ROS that lead to dysfunction and neuronal death. KillerRed is a dimeric red fluorescent protein that produces ROS upon illumination with green light (540-580 nm), thereby inducing cell death[23]. Structurally, KillerRed resembles other fluorescent proteins, such as GFP and RFP[24,25]; however, it is highly toxic due to the presence of a long water-filled channel that allows diffusion of oxygen molecules near the chromophore, providing a path for electron transfer during the production of superoxide radicals[26,27]. The phototoxicity of KillerRed is effective in vivo and can be induced in mammalian and zebrafish cells without co-expression of other factors[23,28]. We have previously shown that KillerRed activation efficiently and specifically kills a variety of neurons in the nematode *C. elegans*, while leaving unaffected the surrounding

[1]Clem Jones Centre for Ageing Dementia Research, Queensland Brain Institute, The University of Queensland, Brisbane, QLD, Australia. [2]School of Biomedical Sciences, Faculty of Medicine, The University of Queensland, Brisbane, QLD, Australia. [3]School of Chemical & Biomolecular Engineering, Georgia Institute of Technology, Atlanta, GA, USA. ✉e-mail: m.hilliard@uq.edu.au

neurons and tissues in which KillerRed is not expressed[29]. This demonstrates the strict cell-autonomy and specificity of KillerRed as a ROS-generating tool. Here, we built an LED (light emitting diode)-driven illumination system (iBox) that allows the simultaneous activation of KillerRed in multiple *C. elegans* populations, a key advantage in performing large scale genetic screens. Using this device, we performed an unbiased forward genetic screen of *C. elegans* expressing KillerRed in six mechanosensory neurons, and identified a transmembrane molecule, T28B8.6 (which we named oxidative stress protective 1 or OSP-1), that protects neurons from ROS-induced damage. Our results revealed that OSP-1 functions cell-autonomously in neurons to protect from ROS-induced damage, and that this protective effect extends to other classes of *C. elegans* neurons as well as to mammalian neurons. We also found that OSP-1 localizes to the endoplasmic reticulum (ER), an organelle that plays a central role in the cellular stress response. Importantly, overexpression of OSP-1 remodels the ER and affects the subcellular positioning of lysosomes, organelles involved in protein degradation and components of the autophagy/lysosomal pathway implicated in neurodegeneration. In line with these observations, we found that acute oxidative stress induces autophagy-dependent cell death, and that overexpressing OSP-1 negatively regulates this process. Overall, our results identify the function of a previously uncharacterized neuroprotective molecule and its cellular mechanism of action, as well as implicate the ER and autophagy in conferring neuronal resistance to oxidative stress.

Results

Development of a multi-illumination platform for KillerRed activation in *C. elegans*

To study how ROS cause neurodegeneration, we focused on the *C. elegans* anterior lateral microtubule (ALM) neurons, as their development, function, maintenance, and regenerative capacity have been well characterized[30–38]. This bilateral pair of mechanosensory neurons mediates avoidance from gentle head touch stimuli, and each has an axon that extends anteriorly along the lateral cord, with a ventral branch which establishes synaptic contacts with other neurons (Fig. 1a). Using a mechanosensory neuron-specific promoter (*pmec-4*), we drove the simultaneous expression of KillerRed (*pmec-4::KillerRed*) and a cytosolic GFP marker (*pmec-4::GFP*) in the ALM neurons, which allowed us to control the generation of ROS with KillerRed and monitor any change in neuronal morphology with GFP (Fig. 1a). Previously described methods for activating KillerRed, using light produced by a fluorescence dissecting microscope, cause efficient oxidative stress-induced cell death detectable by the disappearance of GFP-labeled neurons[29] (Fig. 1b). However, the limited throughput of one population per microscope makes this approach unsuitable for forward genetic screens and laborious for candidate genetic screens. To overcome this limitation, we designed and built an illumination platform named illumination box (iBox), in which twelve LEDs were used as light sources to simultaneously illuminate multiple Petri dishes, each holding a *C. elegans* population (Supplementary Fig. 1a–c). The iBox LEDs were able to efficiently activate KillerRed and kill ALM neurons in both hermaphrodite and male animals (Fig. 1c), thereby closely reproducing our earlier results using the microscope illumination system (~50–60% cell death in ALM neurons)[29]. Importantly, the illumination of animals not carrying the KillerRed transgene did not cause any ALM cell death (*n* = 60). Thus, the iBox can be used to scale-up optogenetic experiments in *C. elegans* and potentially other species, providing an ideal setting for high-throughput genetic screens.

A mutation in *osp-1* enhances KillerRed-induced neurodegeneration

To identify molecules that regulate ROS-induced neurodegeneration, we performed an unbiased forward genetic screen using the iBox and *C. elegans* expressing KillerRed and GFP in the mechanosensory neurons (*pmec-4::KillerRed; pmec-4::GFP*). From this screen, we isolated a recessive mutant allele, *vd60*, that caused higher cell death of ALM neurons after KillerRed activation (Fig. 1d, and Supplementary Fig. 2a, b). Importantly, the mechanosensory neurons of *vd60* mutant animals were morphologically unaffected before illumination (Supplementary Fig. 2c), and with no deficits in their response to gentle touch (Supplementary Fig. 2d). Therefore, the enhanced neurodegeneration observed in these mutants is caused by susceptibility to oxidative stress, and not due to defects in neuronal development.

Through whole-genome sequencing of the *vd60* animals and genetic mapping[39,40], we identified a mutation in the previously uncharacterized gene T28B8.6, residing on the right arm of Chromosome I. The *vd60* mutation in T28B8.6 consists of an A to G transition in position 125 of the coding region (125 A > G) that results in the substitution of the GAG codon (glutamic acid) to a GGG codon (glycine) in position 42 (E42G), which is rarely represented in the genome. Expression of wild-type T28B8.6 under its endogenous promoter (2 kb upstream of the start codon, amplified from genomic DNA) was able to rescue the mutant phenotype of the *vd60* animals, reducing ALM cell death after KillerRed activation to wild-type levels (Fig. 1e). To further investigate the causal role of T28B8.6, we used CRISPR-Cas9 to generate two independent knock-out alleles, *vd98* and *vd99* (see "methods" for details), that removed 86% of the gene. As predicted, this resulted in an enhanced cell death phenotype after oxidative insults (Fig. 1f; Supplementary Table 1).

As increased oxidative stress can affect an animal's lifespan[41], we next asked whether animals carrying mutations in T28B8.6 were short-lived compared to wild-type. *vd60* animals presented with a reduced lifespan compared to wild-type animals, a phenotype that was rescued by the expression of *T28B8.6* under its endogenous promoter (Supplementary Fig. 3a, b).

Taken together, these findings indicate that loss-of-function mutations in *T28B8.6* enhance KillerRed-induced neurodegeneration and increase sensitivity to oxidative stress at the organismal level. Considering these findings, we named the *T28B8.6* locus *osp-1* (oxidative stress protective 1).

OSP-1 acts cell-autonomously to protect neurons from oxidative stress

Computational modeling of OSP-1 functional domains using predictive software (AlphaFold and Phobius, see "methods") indicated that OSP-1 is a transmembrane protein with a signal peptide at the N-terminus, and is predicted to contain three alpha helices and four beta strands (Fig. 2a). The identified *vd60* mutation is predicted to reside in the non-cytoplasmic domain and the second alpha helix (Fig. 2a). To determine the tissue in which OSP-1 is required to protect ALM neurons from ROS-induced damage, we conducted cell- and tissue-specific rescue experiments. ALM neurons are embedded in the skin and, during development, lie close to the muscles (Fig. 2b). We first generated transgenic animals in which the wild-type OSP-1 genomic region was selectively expressed in the six mechanosensory neurons (two ALM neurons plus four other neurons) using the promoter of the gene *mec-4* (*pmec-4::OSP-1*) in the *osp-1(vd60)* animals. We observed a strong rescue of the mutant phenotype in these animals (Fig. 2c), which suggests a cell-autonomous function for OSP-1. As a control, transgenic animals carrying the *mec-4* promoter alone did not show rescue of the oxidative stress-induced cell death (Fig. 2c), confirming that the rescue effect is not due to a promoter titration of transcription factors. In support of a cell-autonomous function, expression of OSP-1 in surrounding tissues, such as the skin (*pdpy-7::OSP-1*) or the muscle (*pmyo-3::OSP-1*), failed to rescue the mutant phenotype (Fig. 2c). Interestingly, overexpression of the mutated version of OSP-1 (*pmec-4::OSP-1(vd60)*) also rescued the KillerRed-induced cell death (Supplementary Fig. 4a), suggesting that the mutated molecule preserves most of its function; this result indicates that the oxidative stress sensitivity of *osp-1(vd60)*
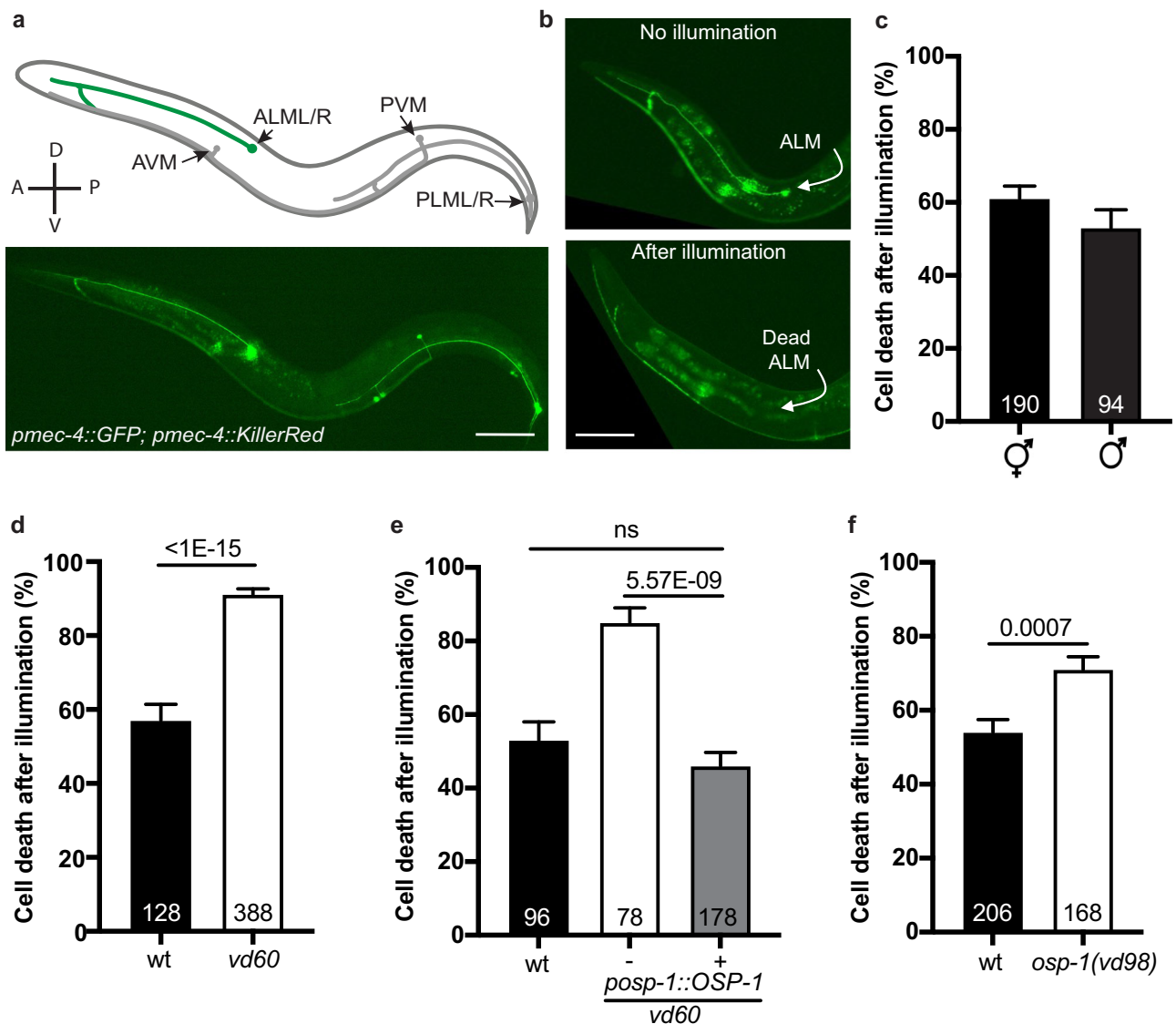
Fig. 1 | *osp-1* mutations enhance oxidative stress-induced neurodegeneration.
a Schematic (top) and epifluorescence image (bottom) of a *C. elegans* animal expressing GFP (*pmec-4::GFP*) and KillerRed (*pmec-4::KillerRed;* not visible in the green channel) in mechanosensory neurons (ALML/R, PLML/R, AVM, and PVM). Scale bar 100 µm. **b** Representative epifluorescence images of an intact ALM neuron in a non-illuminated animal (control, top panel), and a missing (dead) ALM after illumination that activates the KillerRed-induced oxidative stress. Scale bar 100 µm. **c** Quantification of the ALM cell death phenotype in hermaphrodites and males. **d** Quantification of the ALM cell death phenotype in wild-type (wt) and *vd60* mutant animals. Comparisons between groups were done using a two-tailed unpaired t-test. **e** Quantification of the ALM cell death phenotype in wt, and non-transgenic animals (-) and transgenic siblings (+) expressing a wild-type copy of *osp-1* under its endogenous promoter in the *vd60* background. Comparisons between groups were done using one-way ANOVA with a Tukey's test for multiple comparisons. **f** Quantification of the ALM cell death phenotype in wt and *osp-1(vd98)* mutants. Comparisons between groups were done using a two-tailed unpaired t-test. In panels (**c** to **f**), bars represent mean values; *N* values are indicated in the graphs; error bars represent the standard error (SE) of proportion; KillerRed was activated using LED illumination.

mutant animals could be the result of a functional protein being produced at a lower level that can be overcome by overexpression. In support of this notion, we analyzed a CRISPR-Cas9 edited strain in which the glutamate codon in position 42 (GAG) was altered into a glycine using the optimal GGA codon (allele *osp-1(syb2500)*), instead of the synonymous but rare GGG glycine codon present in the *osp-1(vd60)* animals. These animals were not defective, indicating that the glutamate change to glycine per se was not responsible for the increased sensitivity to oxidative stress but rather the specific GGG glycine codon alteration in the *osp-1(vd60)* animals (Supplementary Fig. 4b). To confirm that this was indeed the case, we used CRISPR-Cas9 to recreate the glycine codon GGG of the *vd60* mutant animals, which is the least used in the whole *C. elegans* genome[42,43], in an otherwise non-mutagenized background (alleles *vd228* and *vd230*). As

predicted, these animals presented an increased cell death induced by KillerRed activation (Supplementary Fig. 4c and Supplementary Table 1). Taken together, these results reveal that the *vd60* mutation (GGG codon for glycine) is likely to impair the expression level of OSP-1, thereby causing enhanced cell death upon oxidative stress. They also show that restoring OSP-1 cell-autonomously in the ALM neurons protects them from ROS-induced damage.

The cell-autonomous role of OSP-1 implies that this gene is expressed in the ALM neurons. To confirm this notion, we tagged the C-terminus of *osp-1* with GFP using CRISPR-Cas9 (*osp-1(vd84[osp-1::gfp])*). However, in these animals we could only detect a GFP signal in the germline but not in any somatic cell (Supplementary Fig. 5a). Importantly, the C-terminal tag does not affect OSP-1 function, as the KillerRed-induced cell death in the *osp-1(vd84)* animals was
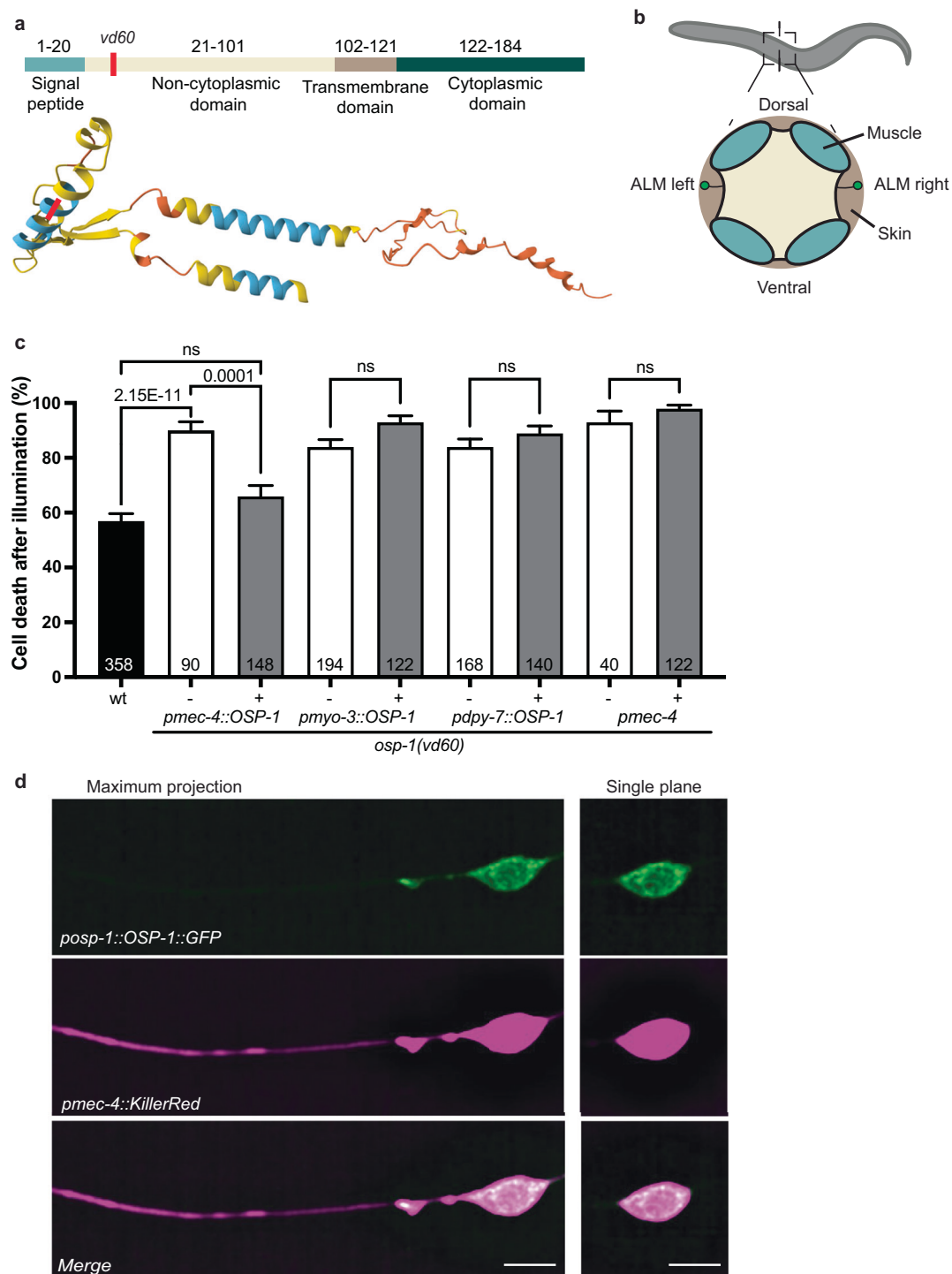
Fig. 2 | *osp-1* acts cell-autonomously to protect neurons from oxidative stress-induced neurodegeneration. a Schematic of OSP-1 organization in protein domains (top) and tertiary structure as predicted using AlphaFold (bottom); light blue represents regions with a high confidence score, yellow represents regions with low confidence, and orange represents regions with very low confidence. **b** Schematic representation of the anatomical location of ALM neurons in the proximity of the skin and the muscles. **c** Quantification of the ALM cell death phenotype in wt and non-transgenic animals (-) and transgenic siblings (+) expressing OSP-1 under the *mec-4* promoter (cell-autonomous), the *myo-3* promoter (muscles), the *dpy-7* promoter (skin), and the promoter alone (*pmec-4*) in the *osp-1(vd60)* background. Bars represent mean values, and comparisons between groups were done using one-way ANOVA with a Tukey's test for multiple comparisons; *N* values are indicated in the graphs; error bars represent the SE of proportion; KillerRed was activated using LED illumination. **d** Deconvolved spinning-disk confocal single-plane images of the ALM neuron expressing OSP-1::GFP under its endogenous promoter (*posp-1::OSP-1::GFP*) and KillerRed under the mechanosensory neuron-specific promoter *pmec-4* (*n* = 43). Left panels are maximum projections and right panels are single planes of the ALM cell body. Scale bars are 5 μm.

indistinguishable from that of wild-type animals (Supplementary Fig. 5b). One possibility is that *osp-1* is expressed at levels too low to detect using an endogenous tag. Therefore, we generated transgenic animals expressing multiple copies of OSP-1::GFP under its own regulatory elements (*posp-1::OSP-1::GFP::3'UTR*) amplified from the genome of *osp-1(vd84[osp-1::gfp])* animals. In these animals, we could detect the expression of OSP-1 in ALM neurons (Fig. 2d). We also found OSP-1 expression in five other bilateral pairs of neurons: the PLM and the PHA neurons in the tail, the head RIA interneurons, and two bilateral pairs of head neurons that, based on location and morphology, appeared to be URA ventral and dorsal (Supplementary Fig. 5c–f). These results conclusively demonstrate that OSP-1 is expressed at very low levels in somatic cells, and that it is present in ALM and other neurons.

According to RNA sequencing and tiling array studies, OSP-1 is upregulated in conditions such as bacterial infection with *Enterococcus faecalis* and *Bacillus thuringiensis*[44,45] and downregulated upon treatment with the antibiotic triclosan[46], suggesting a potential regulation by stress. To investigate whether *osp-1* is upregulated under acute oxidative stress we activated KillerRed in the transgenic animals described above in which *osp-1* is tagged with GFP and expressed under its own regulatory elements (*posp-1::OSP-1::GFP::3'UTR*). Our results revealed an increase in OSP-1::GFP intensity after KillerRed-induced oxidative stress (Supplementary Fig. 6a, b). Taken together, these data reveal that OSP-1 functions cell-autonomously in ALM neurons, is expressed at low levels, and can be induced by an acute oxidative insult.

OSP-1 protects different *C. elegans* neuronal types as well as mammalian cells from different oxidative insults

To determine whether OSP-1 overexpression could enhance the resistance of wild-type animals to ROS-induced neurodegeneration, we overexpressed OSP-1 under its endogenous promoter. Our results revealed that the cell death of ALM neurons after KillerRed activation was significantly reduced compared to that of wild-type animals (Fig. 3a). We then asked whether overexpression of OSP-1 could also protect a different class of *C. elegans* neurons from other neurodegenerative insults. To investigate this aspect, we turned to an established model of dopaminergic neurodegeneration. The *C. elegans*

dopaminergic neurons are a set of eight cells, two located in the midbody and six in the head of the animal (four CEP neurons and two ADE neurons) (Fig. 3b). The degeneration of these neurons has been studied in the context of Parkinson's disease, a condition in which oxidative stress is a central component and that has been well modeled in *C. elegans*[47–53]. Previous work has revealed that, similar to the mammalian systems, the *C. elegans* head dopaminergic neurons are sensitive to the neurotoxin 6-hydroxydopamine (6-OHDA) and degenerate upon incubation with this chemical[48,50,52]. To determine the potential of OSP-1 to confer protection to dopaminergic neurons, we generated a transgenic strain that expresses the wild-type genomic region of *osp-1* under the dopaminergic-specific promoter *dat-1* (*pdat-1::OSP-1*). These animals also carry a transgene for the visualization of the dopaminergic neurons with GFP (*pdat-1::GFP*). To control for non-specific effects due to the overexpression of the *dat-1* promoter itself, we expressed mCherry in the dopaminergic neurons (*pdat-1::mCherry*). Remarkably, overexpression of OSP-1, but not mCherry, led to an increase in intact dopaminergic neurons after treatment with 6-OHDA, demonstrating that OSP-1 protects these neurons from 6-OHDA-induced neurodegeneration (Fig. 3c). We also investigated the ability of OSP-1 to confer protection from oxidative stress to mammalian neurons. To assess this, we triggered oxidative stress in neuronal-like rat pheochromocytoma cells (PC12) by exposing them to hypoxia for 24 h[54], after which we evaluated cell death based on the presence of pyknotic nuclei (Fig. 4a). Transfection with a codon-optimized version of OSP-1 tagged with GFP was able to suppress the hypoxia-induced neurodegeneration (Fig. 4b). Similarly, transfection of human neuroblastoma cells (SH-SY5Y) with OSP-1 was able to protect them from hypoxia-induced cell death (Fig. 4c, d). Together, these results demonstrate that overexpression of OSP-1 protects various classes of nematode neurons from different types of oxidative insults, and exerts a neuroprotective effect in mammalian cells.

OSP-1 localizes to and remodels the endoplasmic reticulum

To further investigate OSP-1 subcellular localization and function, we generated a functional, fluorophore-tagged version of OSP-1 selectively expressed in the mechanosensory neurons (*pmec-4::OSP-1::GFP*) (Supplementary Fig. 7a). As with the endogenous promoter, we
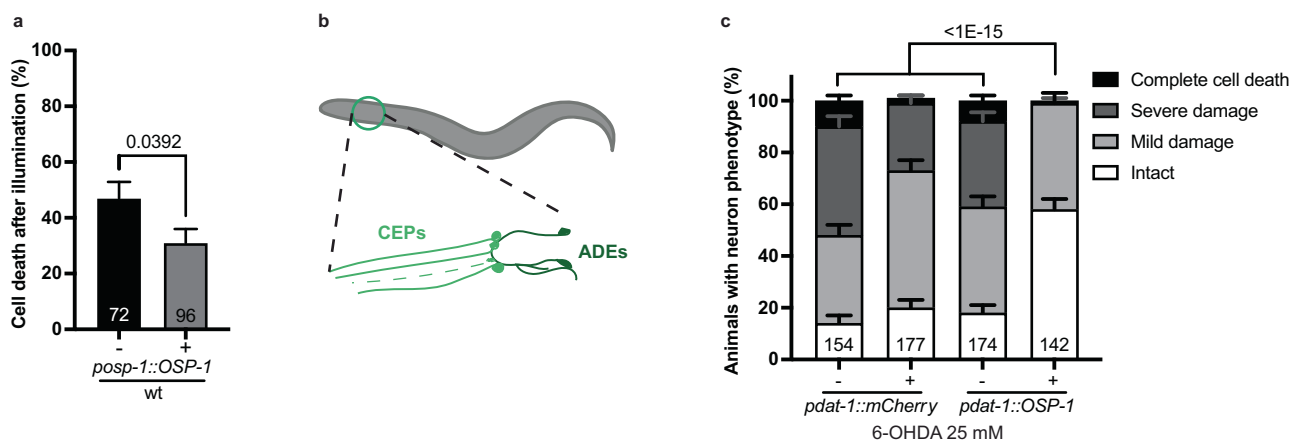

Fig. 3 | OSP-1 overexpression protects mechanosensory neurons and dopaminergic neurons from oxidative stress-induced neurodegeneration.
a Quantification of the ALM cell death phenotype in non-transgenic animals (-) and transgenic siblings (+) overexpressing OSP-1 under its endogenous promoter (*posp-1::OSP-1*) in the wt background. Bars represent mean values, and comparisons between groups were done using a two-tailed unpaired t-test; *N* values are indicated in the graph; error bars represent the SE of proportion; KillerRed was activated using LED illumination. **b** Schematic representation of the morphology and anatomical location of the head dopaminergic neurons, including the four cephalic sensilla (CEP) neurons and two anterior deirid (ADE) neurons. **c** Quantification of

neuronal damage and death 48 h after 1.5 h treatment with 6-OHDA (25 mM) in transgenic animals (+) expressing either mCherry or OSP-1 under the *dat-1* promoter. Wild-type non-transgenic siblings (-) were used as controls. Animals possessing all neurons (ADE + CEP) were scored as "intact" (white bar), those with partial loss of CEP but intact ADE neurons as "mild damage" (light gray bar), those with complete loss of CEP but intact ADE neurons as "severe damage" (dark gray bar) and the rest as "complete cell death" (black bar). Bars represent mean values, and comparisons between groups were done using two-way ANOVA with a Tukey's test for multiple comparisons; *N* values are indicated in the graph; error bars represent the SE of proportion.
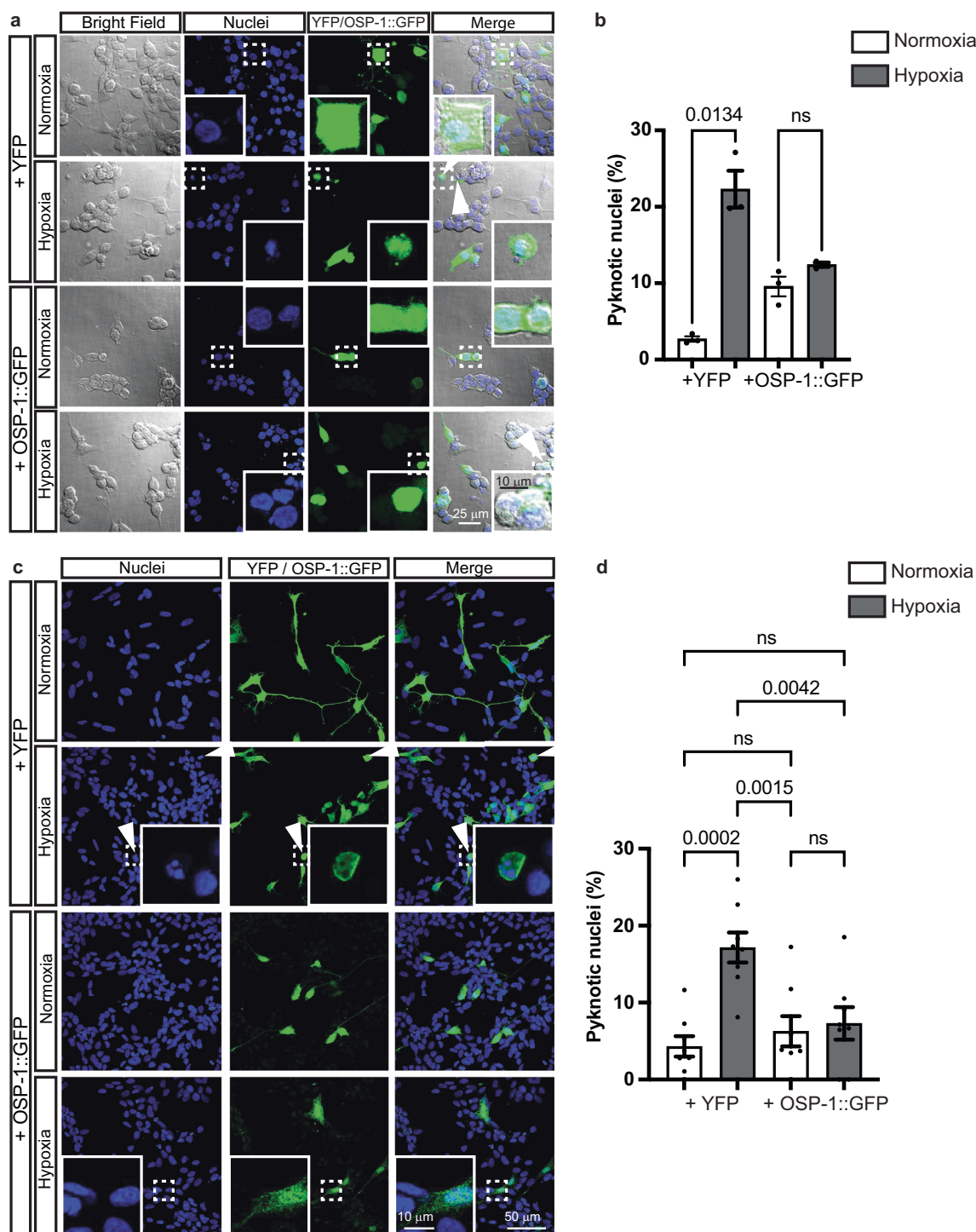
Fig. 4 | OSP-1 protects mammalian cells from hypoxia-dependent oxidative insult. a PC12 cells transfected with YFP or OSP-1::GFP in either normoxic or hypoxic conditions. White arrowhead indicates pyknotic nuclei caused by hypoxia. Scale bars are 25 μm in the main panels and 10 μm in the insets. **b** Hypoxia causes degeneration of PC12 cells transfected with YFP but not with OSP-1::GFP, as observed by counting pyknotic nuclei. The experiments were performed in triplicate; error bars represent the SE of the mean (SEM); comparisons between groups were done using the Kruskal-Wallis test adjusted for multiple comparisons (Dunn's test). **c** SH-SY5Y cells transfected with YFP or OSP-1::GFP in either normoxic or hypoxic conditions. White arrowhead indicates pyknotic nuclei caused by hypoxia. Scale bars are 50 μm in main panels and 10 μm in the insets. **d** Hypoxia causes degeneration of SH-SY5Y cells transfected with YFP but not with OSP-1::GFP, as observed by counting pyknotic nuclei. The experiments were performed in triplicate and repeated three times; error bars represent the SEM; comparisons between groups were done using one-way ANOVA with a Tukey's test for multiple comparisons. In panels (**b** and **d**) bars represent mean values; each dot represents an individual experiment.

observed that OSP-1 specifically localized to intracellular membranes and around the nucleus, in a pattern that resembled the ER (Fig. 5a). To confirm this observation, we generated single-copy insertions of *pmec-4::OSP-1::GFP*, *vdSi44* and *vdSi46* (which is functional), (Supplementary Fig. 7b), and visualized OSP-1::GFP together with an RFP-tagged version of MEC-6 (*pmec-6::MEC-6::tagRFP*), an ER-residing paraoxonase-like protein[55]. OSP-1::GFP strongly colocalized with MEC-6::RFP in the cell body of ALM neurons (Fig. 5b, d), as early as during the first larval stage (L1) (Fig. 5e, f); as a control, OSP-1 did not colocalize with mitochondria (labeled with the *pmec-4::TOMM-20::RFP* transgene) (Fig. 5c, d). However, unlike MEC-6::RFP but similar to YFP::PISY-1 (an ER-resident phosphatidyl transferase; *pmec-4::YFP::PISY-1*), OSP-1::GFP was also present in the neurite of ALM (Supplementary Fig. 7c).

We next investigated the effects of the OSP-1 mutation or over-expression on ER morphology in animals expressing YFP::PISY-1 to visualize the ER. Using super-resolution microscopy, we identified a branched appearance of the axonal ER and observed that the *osp-1(vd60)* mutation reduced this branching in the proximal segment (Fig. 6a, b). Conversely, overexpression of *pmec-4::OSP-1* led to an accumulation of ER in the proximal region of the ALM axon (Fig. 6c, d). Three lines of evidence indicate that this rearrangement of the ER is a specific effect of OSP-1, and not the result of the overexpression of any ER-resident molecule. First, both reporters used to visualize the ER (YFP::PISY-1 and MEC-6::RFP) expressed these ER molecules at high levels, and neither of them induced ER rearrangement[55]. Second, we did not observe this phenotype in animals overexpressing an additional ER-residing molecule, the E3 ubiquitin-protein ligase SEL-11/HRD1, or the *pmec-4* promoter alone (Fig. 6c, d). Third, this effect was also observed when OSP-1 was cell-autonomously expressed at a lower concentration, or under its endogenous promoter (Supplementary Fig. 8a, b). To ensure that the phenotype we observed is a true ER rearrangement rather than a specific alteration of PISY-1 localization, we used two additional ER markers, MEC-6::tagRFP and OSP-1::GFP, and in both cases found a similar ER proximal accumulation when OSP-1 was overexpressed (Supplementary Fig. 8c, d). It is important to note that overexpressing the mutated OSP-1 in ALM neurons (*pmec-4::OSP-1(vd60)*) also induces ER arrangement (Supplementary Fig. 8e), in line with the notion that mutated OSP-1 is functional and has an effect in an overexpressing context.

We then asked whether the OSP-1-driven proximal ER accumulation disrupted axon transport. To address this question, we used a previously characterized reporter for axonal transport in the mechanosensory neurons consisting of Kinesin-3/UNC-104 tagged with GFP (*pmec-4::UNC-104::GFP*)[34,56]. This marker typically accumulates at the distal axon tip (Fig. 6e), a distribution that was not affected by OSP-1 overexpression or mutation (Fig. 6e, f).

Together, these data suggest that OSP-1 regulates ER organization but does not impair axonal transport.

OSP-1 regulates the distribution of lysosomes

The ER is an important organelle that is involved in several cellular processes including protein synthesis, lipid biogenesis, calcium metabolism, autophagosome formation, and the maintenance of cellular homeostasis in response to stress[57–59]. It is also known to interact with other organelles as well as protein complexes such as 26S proteasomes, which cluster in microcompartments at specific ER hot spots[60]. Given that the proteasome is responsible for degrading and removing oxidized and damaged proteins targeted for degradation[61–63], we asked whether OSP-1 regulates proteasomal function and interactions with the ER membrane, in which case we would expect OSP-1 to colocalize with proteasomes in the ALM neurons. To test this hypothesis, we first visualized the α1 proteasome subunit PSMA1/PAS-6 using a single-copy insertion of a functional PAS-6 tagged with RFP expressed specifically in the mechanosensory neurons (*pmec-4::PAS-6::linker::RFP*) together with an OSP-1::GFP single-

copy insertion. In these animals, we observed that PAS-6::RFP localized to the nucleus as well as intracellular structures surrounding the nucleus and along the axon (Supplementary Fig. 9a). In addition, OSP-1::GFP only weakly colocalized with PAS-6::RFP with a correlation score of 0.4, which was not altered in the *osp-1(vd60)* background (Supplementary Fig. 9b). Moreover, neither the distribution of PAS-6::RFP in the cell body or the number or size of PAS-6::RFP puncta along the axon were visibly affected by mutation or overexpression of OSP-1::GFP when compared to wild-type (Supplementary Fig. 9c, d). This suggests that OSP-1 does not interact with the proteasome and does not affect proteasomal localization in the mechanosensory neurons.

The ER also interacts with lysosomes, single-membrane organelles whose dysfunction is implicated in cellular damage and neurodegeneration[64–67]. To explore the effect of OSP-1 mutation and overexpression on these organelles, we visualized lysosomes by tagging the lysosomal protein CTNS-1 with mCherry (*pmec-4::CTNS-1::mCherry*). This marker confirmed previous observations that lysosomes are predominantly located in the cell body, where they execute their endocytic and autophagic degradative function, but can also be found in the proximal segment of the axon (Fig. 7a)[68–70]. We observed a clustering of CTNS-1::mCherry proximal to the cell body in *osp-1(vd60)* mutant animals, which was rescued by cell-autonomous expression of wild-type *osp-1* (Fig. 7b). Moreover, animals overexpressing OSP-1 had more dispersed lysosomes along the axon compared to both wild-type and *osp-1(vd60)* mutant animals (Fig. 7c), and a lower presence of lysosomes in the cell body (based on fluorescence intensity) (Fig. 7d). However, the size and circularity of these lysosomes did not vary amongst the genotypes analyzed (Supplementary Fig. 10a–c), and mutant animals did not display any difference in mitochondrial distribution compared to wild-type (Supplementary Fig. 10d–g). These data suggest an alteration of lysosome distribution in *osp-1(vd60)* mutant animals that could be indicative of a protein degradation defect and oxidative stress sensitivity in this background. They also indicate that the increased presence of lysosomes in the axon could be part of the neuroprotective mechanism conferred by overexpression of OSP-1.

Autophagy inhibition protects neurons from oxidative stress-induced neurodegeneration

Lysosomes are key elements of the proteolytic system represented by the autophagy/lysosomal pathway. It has also been shown that lysosome positioning and clustering affect autophagy. In particular, peripherally dispersed lysosomes in nutrient-rich conditions lead to mTOR activation and autophagy inhibition, whereas starvation-induced perinuclear clustering reduces mTOR function, thereby activating autophagy[71]. We hypothesized that the increase in lysosomes in the cell body of *osp-1(vd60)* mutant animals could indicate an increase in autophagy, whereas a decrease in the cell body with axonal dispersion of lysosomes in the OSP-1-overexpressing animals could indicate an inhibition of autophagy, thereby explaining the neuroprotective effect of this transgene. If true, animals in which autophagy is inhibited should exhibit reduced cell death after oxidative stress. To test this hypothesis, we used a mutant in the serine/threonine protein kinase UNC-51/ULK1, an Atg1 ortholog required for autophagosome formation[72] (Fig. 8a), and tested its effect in our KillerRed-induced cell death paradigm. Remarkably, two mutant alleles of *unc-51*, *e369* and *e1189*, led to reduced cell death after oxidative stress (Fig. 8b). To confirm that this was a specific effect, we introduced a wild-type copy of *unc-51* driven by its endogenous promoter (*punc-51::UNC-51*) and found that it could rescue the cell death phenotype (Fig. 8c). *unc-51* animals carrying a single-copy insertion of the wild-type *unc-51* gene under the mechanosensory-specific promoter *pmec-7* (*pmec-7::UNC-51*)[73] also presented a full rescue of the cell death phenotype (Fig. 8d), demonstrating that UNC-51 functions cell-autonomously within the ALM neurons. However, neither endogenous
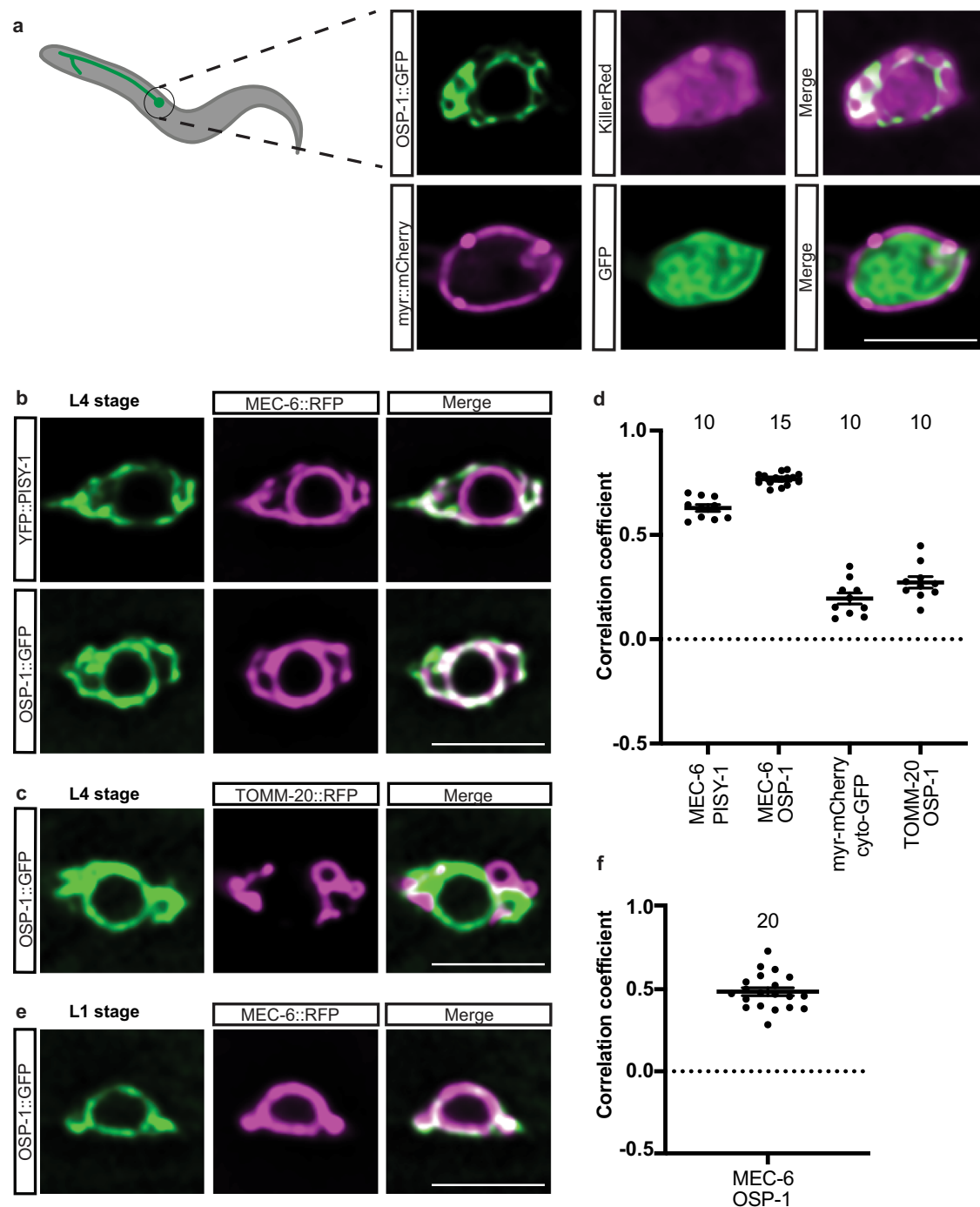
Fig. 5 | OSP-1 localizes to the ER membrane. a Deconvolved spinning-disk confocal single-plane images of the ALM cell body in a representative 1-day-old adult animal (1DOA) expressing a functional OSP-1::GFP and KillerRed under the mechanosensory-specific promoter (*pmec-4*) (top panel; *n* = 11). The localization of OSP-1 appears to be intracellular and differs from that of plasma membrane molecules such as myristoylated mCherry (myr::mCherry) and cytosolic GFP under the *pmec-4* promoter (bottom panel; *n* = 8). **b** Deconvolved spinning-disk confocal single-plane images of the ALM cell body in a representative animal (L4 stage) expressing the ER markers YFP::PISY-1 and MEC-6::tagRFP under the mechanosensory neuron-specific promoters *pmec-4* and *pmec-6*, respectively (top panel, *n* = 10), or expressing a miniMos insertion of OSP-1::GFP and the ER marker MEC-6::tagRFP under the *pmec-4* and *pmec-6* promoters, respectively (bottom panel,

n = 15). **c** Deconvolved spinning-disk confocal single-plane images of the ALM cell body in a representative animal (L4 stage) expressing the miniMos insertion of OSP-1::GFP and the mitochondrial marker TOMM-20::RFP under the *pmec-4* promoter (*n* = 10). **d** Colocalization analysis and correlation coefficients. Measures of center represent mean values; every dot represents one animal; error bars are SEM. **e** Deconvolved spinning-disk confocal single-plane images of the ALM cell body of a representative animal expressing a miniMos insertion of OSP-1::GFP and the ER marker MEC-6::tagRFP under *pmec-4* and *pmec-6* promoters, respectively (first larval stage, *n* = 20). **f** Colocalization analysis in L1 animals. Measures of center represent mean values; each dot represents one animal, and the error bars are SEM. In all panels, scale bars are 5 µm.
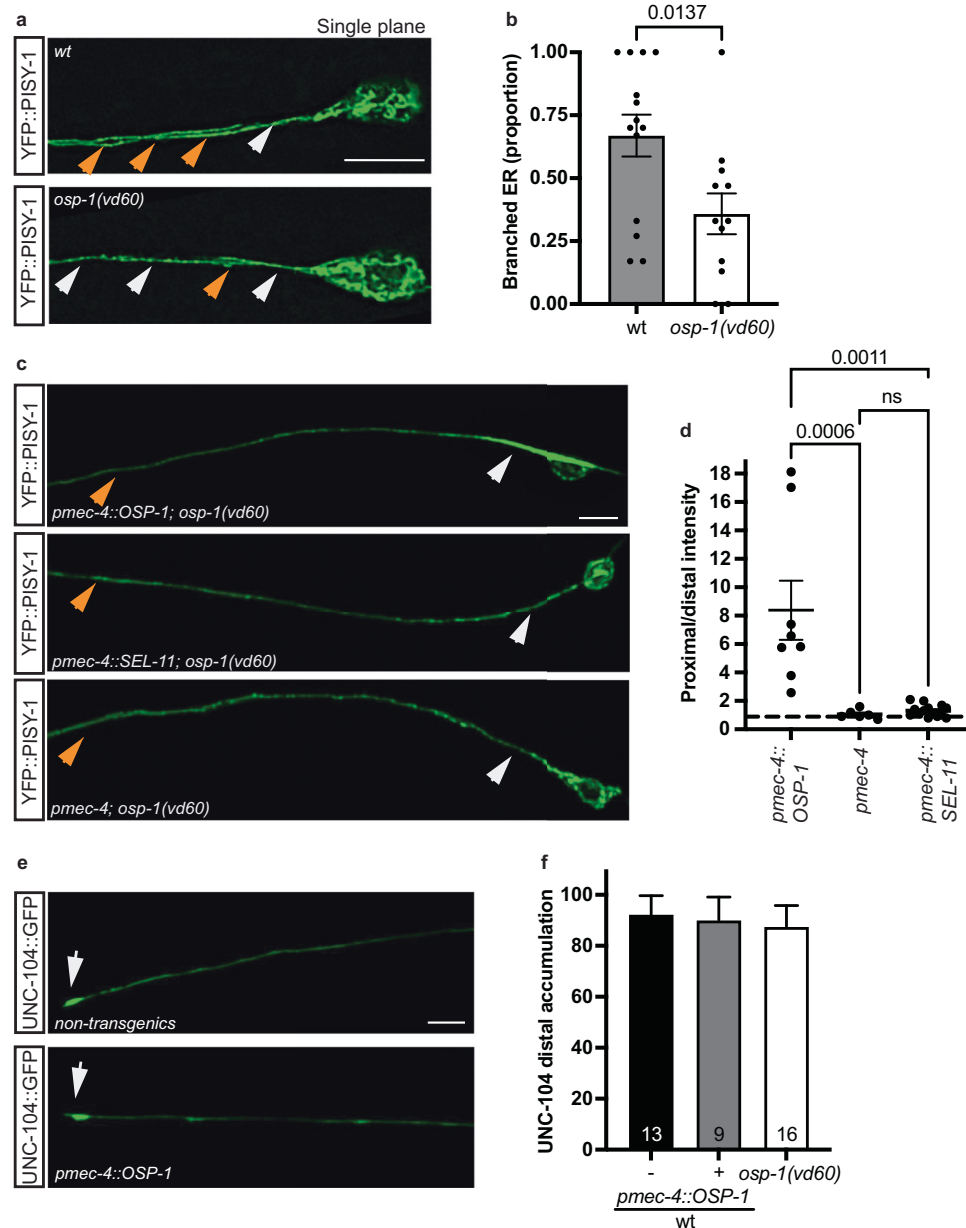
Fig. 6 | OSP-1 remodels the ER. a Deconvolved two-photon confocal images of an ALM neuron expressing YFP::PISY-1 to visualize the ER in both the wt and *osp-1(vd60)* background. Orange arrows indicate branched regions of the axonal ER; white arrows indicated unbranched regions. **b** Measure of the proportion of branched versus unbranched ER in the proximal axonal segment (15 μm) in wt (*n* = 14) and *osp-1(vd60)* animals (*n* = 12). Bars represent mean values; comparisons between groups were done using a two-tailed unpaired t-test; each dot represents an animal; error bars are SEM. **c** Deconvolved spinning-disk confocal maximum projection of an ALM neuron in which the ER is labeled with YFP::PISY-1 and expressing *pmec-4::OSP-1* (untagged), *pmec-4* only or *pmec-4::SEL-11*. Only *pmec-4::OSP-1* overexpression causes an ER accumulation in the proximal region of the neurite as indicated by the white arrow. **d** Quantification of the GFP intensity as a ratio between the proximal region (within the first 10 μm from the cell body, white arrow in panel (**c**) and a more distal region (40 μm downstream from the cell body,

orange arrow in panel (**c**) in animals in which the ER is visualized with YFP::PISY-1 and expressing *pmec-4::OSP-1* (*n* = 8), *pmec-4* only (*n* = 6) or *pmec-4::SEL-11* (*n* = 14). Measures of center represent mean values; each dot represents one animal, and the error bars are SEM. Comparisons between groups were done using the Kruskal-Wallis test adjusted for multiple comparisons (Dunn's test). **e** Deconvolved spinning-disk confocal maximum projection of an ALM neuron distal tip showing the distribution of UNC-104::GFP (white arrow) as a marker for neuronal transport. **f** Quantification of the percentage of neurons showing a the distribution of UNC-104::GFP in *osp-1(vd60)* animals and in non-transgenic animals (-) and transgenic siblings (+) overexpressing *pmec-4::OSP-1* in the mechanosensory neurons (untagged) in the wt background. *N* values are indicated in the graph; error bars represent the SE of proportion. Bars represent mean values, and comparisons between groups were done using one-way ANOVA with a Tukey's test for multiple comparisons. In panels (**a**, **c** and **e**) scale bars are 5 μm.

nor cell-autonomous overexpression of UNC-51 in wild-type animals affected oxidative stress-induced cell death (Fig. 8c, d).

Although UNC-51 is a primary initiator of autophagy, it also has autophagy-independent functions such as axon elongation and guidance[74–76]. To test whether the reduced cell death observed in the *unc-51* mutant animals was specifically due to its role in autophagy, we

tested animals carrying a mutation in another molecule required for autophagosome biogenesis - the autophagy-related gene 13, *atg-13/ATG13* (Fig. 8a). Under KillerRed-induced oxidative stress, *atg-13* mutant animals exhibited reduced ALM neuronal death, thereby mimicking the *unc-51* phenotype (Fig. 8e). This indicates that the effects observed in the *unc-51* mutant background are indeed the
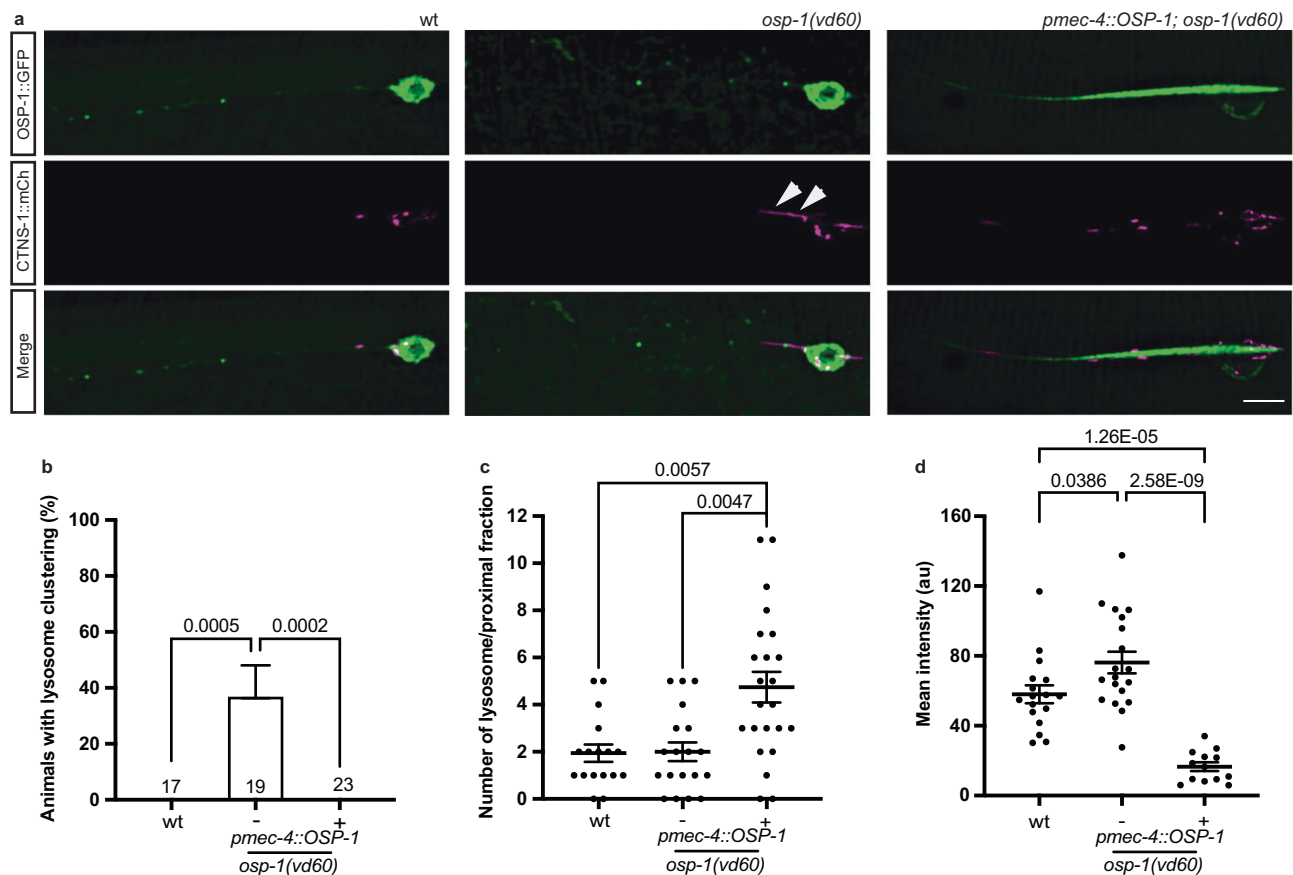
Fig. 7 | OSP-1 controls lysosome positioning in ALM neurons, with its over-expression redistributing lysosomes to the periphery. a Deconvolved spinning-disk maximum projection of ALM neurons in which the ER is labeled with OSP-1::GFP (single-copy insertion *vdSi44*) and expressing *pmec-4::CTNS-1::mCherry* to visualize lysosomes in wt, and non-transgenic animals (-) and transgenic siblings (+) overexpressing OSP-1 (*pmec-4::OSP-1*) in the *osp-1(vd60)* background. White arrows indicate clustering of lysosomes near the cell body in *osp-1(vd60)* animals. Scale bar 5 μm. **b** Penetrance of the proximal lysosome clustering phenotype in the above-mentioned genotypes. Bars represent mean values, and comparisons between groups were done using one-way ANOVA with a Tukey's test for multiple

comparisons; *N* values are indicated in the graph; error bars represent the SE of proportion. **c** Number of lysosomes in the proximal region of the ALM neurite in the abovementioned genotypes. Comparisons between groups are done using the Kruskal-Wallis test adjusted for multiple comparisons (Dunn's test). **d** Lysosome intensity in the cell body of ALM neurons in the abovementioned genotypes. Comparisons between groups were done using one-way ANOVA with a Tukey's test for multiple comparisons. In panels (**c** and **d**) measures of center represent mean values; each dot represents one animal wt (*n* = 17), non-transgenic animals (-; *n* = 19), transgenic siblings (+; *n* = 23), and error bars are SEM.

results of impaired autophagy and not due to axonal misguidance. We then tested whether impairing autophagy at a later stage of autophagosome formation, such as the elongation phase, also reduced oxidative stress-induced cell death. ATG-3 is a molecule that is important for phagophore elongation[77,78], and animals with an ATG-3 mutation presented with lower cell death compared to that of wild-type controls when exposed to oxidative stress (Fig. 8f). Blocking the completion of the autophagic process using chloroquine, which inhibits the fusion of the lysosomes with the autophagosomes (Fig. 8a), was also able to reduce the KillerRed-induced cell death (Fig. 8g). Although these data support the requirement of autophagy during the cellular demise initiated by oxidative stress, we sought to determine whether other cell death pathways are also involved. We have previously shown that KillerRed-induced cell death is independent of the apoptotic caspase CED-3[29]. We therefore tested the effect of mutating a necrosis-specific gene, the calpain gene *clp-1*[79], and observed that, similar to *ced-3* mutants, the resultant animals failed to suppress KillerRed-induced degeneration (Supplementary Fig. 11a). Similarly, animals carrying mutations in both *clp-1* and *ced-3* also failed to exhibit suppression of cell death after KillerRed activation (Supplementary Fig. 11b). Taken together, these data support a specific role for autophagy in the degenerative process and suggest that the inhibition of autophagy is protective against acute ROS-induced neuronal damage.

OSP-1 inhibits autophagy

Having established autophagy as a mode of cell death after oxidative stress, we sought to test the role of OSP-1 in autophagy. First, we asked whether *osp-1* and *unc-51* function in the same pathway. To address this notion, we generated *osp-1; unc-51* animals and demonstrated that these double mutants displayed the same level of KillerRed-induced cell death as animals carrying an *unc-51* mutation alone, suggesting that UNC-51 is epistatic to OSP-1 and that UNC-51 is required for the increased susceptibility to cell death that is observed in *osp-1* mutant animals (Fig. 9a). To further test the effect of OSP-1 on autophagy, we used a fluorescent *mCherry::GFP::LGG-1* reporter that allowed us to measure autophagy in the mechanosensory neurons (*pmec-7::mCherry::GFP::LGG-1*)[73]. Using this reporter, autophagosomes appear as both GFP- and mCherry-positive puncta (yellow). When autophagosomes fuse with lysosomes to complete the degradation of their content, the lower pH quenches GFP and the resulting autolysosomes are visible as mCherry-positive/GFP-negative puncta (red) (Fig. 9b). In *unc-51* mutants, we observed a significantly reduced level of autolysosomes compared to that in wild-type animals, measured as the fluorescence intensity of the ALM cell body, in line with the reduced levels of autophagy in these mutants (Fig. 9c, d). Similar to *unc-51* animals, OSP-1 overexpressing animals, which are neuroprotected,
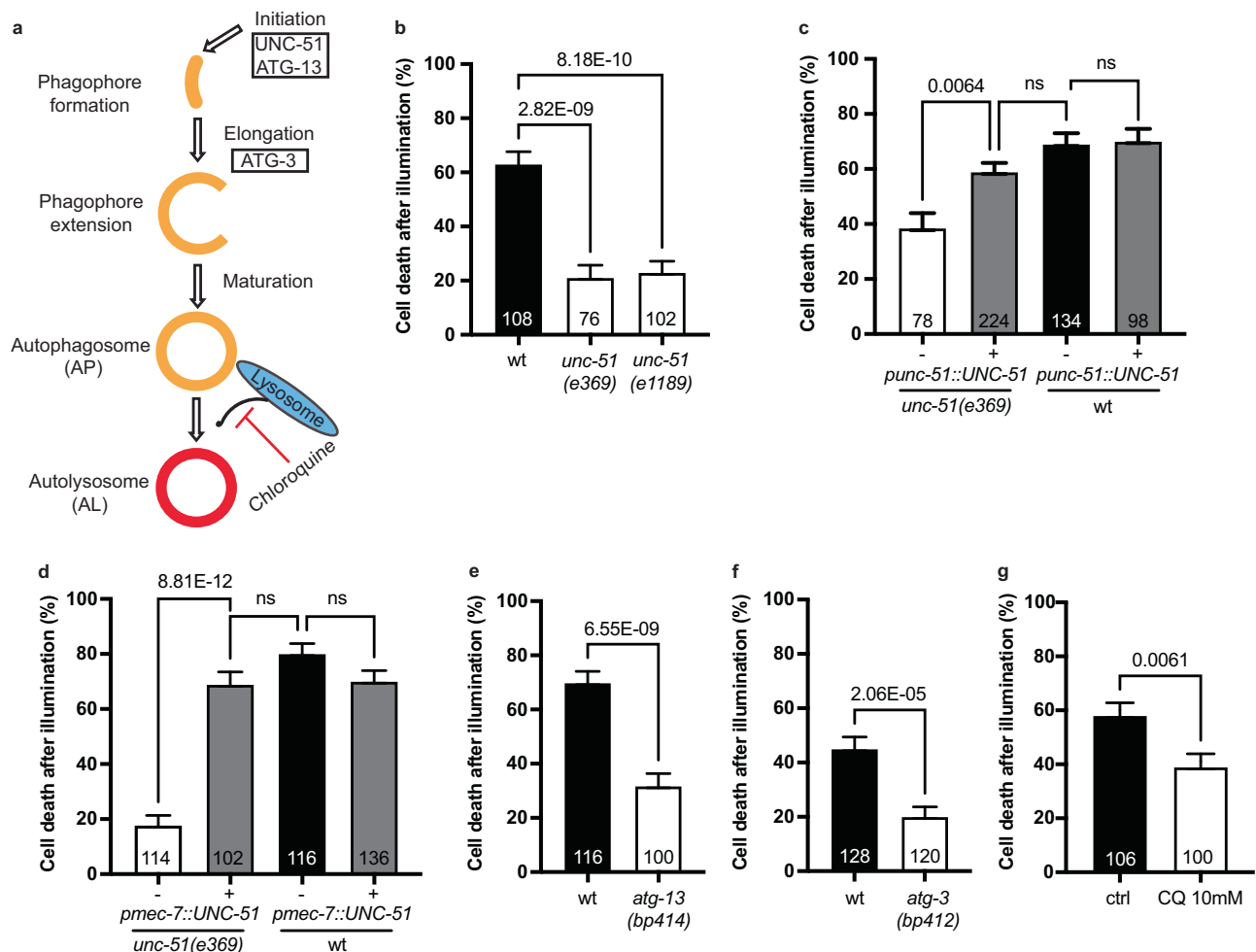
Fig. 8 | Blocking autophagy protects ALM neurons against oxidative stress.
a Schematic representation of autophagosome biogenesis with molecules that act in the initiation and elongation stages. Autophagosomes then fuse with lysosomes to form autolysosomes, a process that is inhibited by chloroquine. **b** Quantification of the ALM cell death phenotype in wt and animals expressing two *unc-51* alleles (*e369* and *e1189*). **c** Quantification of the ALM cell death phenotype in non-transgenic (-) and transgenic (+) animals expressing UNC-51 under its endogenous promoter (*punc-51::UNC-51*) in either *unc-51(e369)* or wt background.
d Quantification of the ALM cell death phenotype in non-transgenic animals (-) and transgenic siblings (+) expressing UNC-51 specifically in the mechanosensory neurons (*pmec-7::UNC-51*) in either *unc-51(e369)* or wt background. In panels (**b**–**d**), comparisons between groups were done using one-way ANOVA with a Tukey's test for multiple comparisons. **e** Quantification of the ALM cell death phenotype in wt and *atg-13(bp414)* animals. **f** Quantification of the ALM cell death phenotype in wt and *atg-3(bp412)* animals. **g** Quantification of the ALM cell death phenotype in animals illuminated on control plates (H_2O) versus plates containing 10 mM chloroquine (CQ). In panels (**e**–**g**) comparisons between groups were done using a two-tailed unpaired t-test. In panels b to g, bars represent mean values; *N* values are indicated in the graphs; error bars represent the SE of proportion, KillerRed was activated using microscope illumination.

displayed a decreased level of autolysosomes fluorescence (Fig. 9c, d), confirming our previous findings of reduced somatic lysosomal content (as observed with the lysosomal marker CTNS-1::mCherry). Moreover, *osp-1(vd60)* mutant animals exhibited a moderate increase in autolysosomes compared to wild-type animals, pointing to an enhanced autophagy state (Fig. 9d). These data suggest that OSP-1 might inhibit autophagy, potentially affecting neuronal vulnerability to oxidative stress-induced damage. If this is true, we would also expect to find that proteins which are normally degraded by autophagy instead accumulate in *unc*-51 mutants, as well as when OSP-1 is overexpressed. To test this notion, we monitored the degradation of SQST-1, a known substrate of autophagy[80]. Animals expressing GFP-tagged SQST-1 under its endogenous promoter (*psqst-1::SQST-1::GFP*)[81] have a basal level of fluorescence that is readily detectable in neurons (Supplementary Fig. 12a). In animals with mutated *unc-51*, there is a global increase in the reporter as it is no longer degraded by autophagy (Supplementary Fig. 12b). When we measured SQST-1::GFP levels cell-specifically in ALM neurons we observed that OSP-1 overexpression also increased the fluorescence

of the reporter, a result that is consistent with an inhibition of autophagy (Fig. 9e, f). To further explore the effect of *osp-1* mutation on SQST-1::GFP accumulation we induced oxidative stress by activating KillerRed in wild-type and *osp-1(vd60)* animals; however, similar to the moderate increase in autolysosomes presented earlier (Fig. 9d), we observed only a minor trend for reduced SQST-1::GFP in mutant animals (Supplementary Fig. 12c). It remains to be determined whether OSP-1 can also have an impact on the autophagy flux.

Overall, these results suggest that overexpression of OSP-1 may negatively modulate autophagy, potentially contributing to the protection of neurons from oxidative stress-induced degeneration (Fig. 10).

Discussion
In this study, we adopted the nematode *C. elegans* as an in vivo multicellular model system and discovery platform to identify a molecule that protects neurons from oxidative stress-induced degeneration. Oxidative stress is a common denominator for neurodegenerative
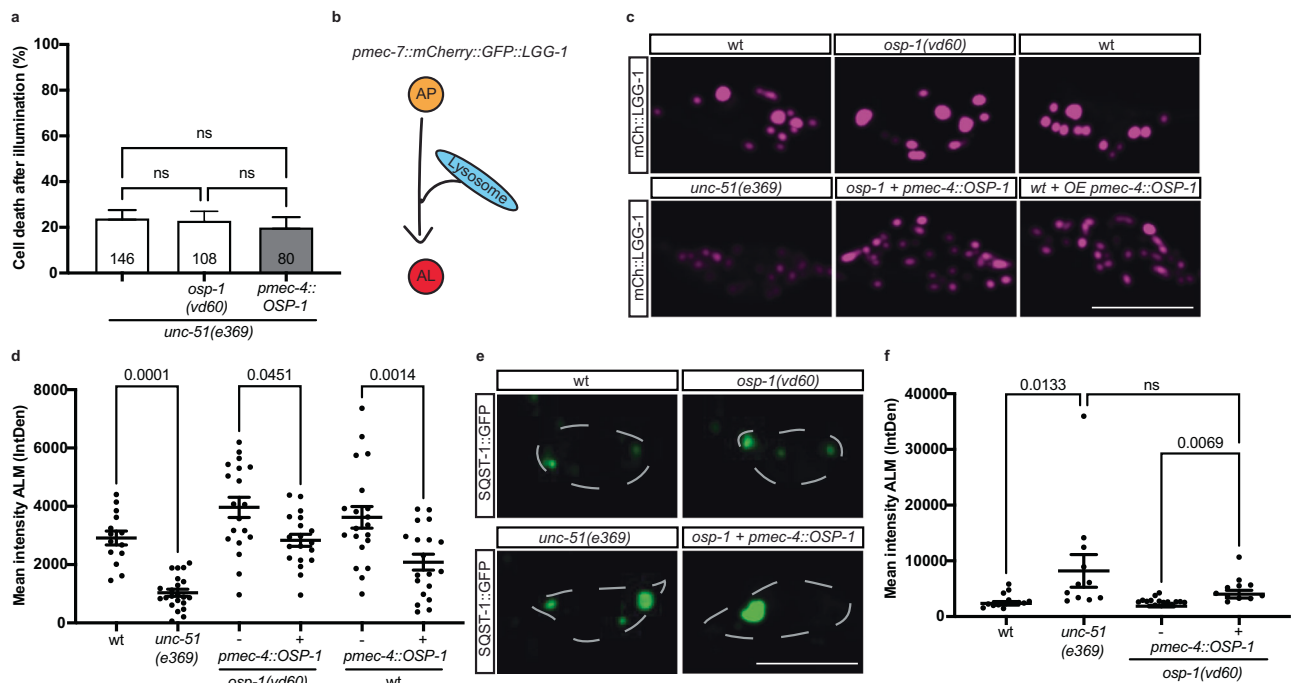
Fig. 9 | OSP-1 acts upstream of *unc-51* and inhibits autophagy. a Quantification of the ALM cell death phenotype in *unc-51* animals with mutation or overexpression of OSP-1. *N* values are indicated in the graph; error bars represent the SE of proportion; bars represent mean values, and comparisons between groups were done using one-way ANOVA with a Tukey's test for multiple comparisons; KillerRed was activated using microscope illumination. **b** Schematic representation of the fluorescence emitted by the dual reporter mCherry::GFP::LGG-1 in autophagosomes (APs) and autolysosomes (ALs). **c** Deconvolved spinning-disk confocal maximum projection of an ALM neuron expressing the autophagy marker mCherry::GFP::LGG-1 under a mechanosensory-specific promoter (*pmec-7::mCherry::GFP::LGG-1*) in wt and *unc-51* (left panels), non-transgenic animals and transgenic siblings expressing *pmec-4::OSP-1* in the *osp-1(vd60)* background (middle panels), as well as non-transgenic animals and transgenic siblings expressing *pmec-4::OSP-1* in the wt background (right panels). Scale bar 5 µm. **d** Quantification of the AL fluorescence in the ALM cell bodies in the following genotypes: wt (*n* = 14), *unc-*

51(e369) (*n* = 22), non-transgenic animals (-; *n* = 19) and transgenic siblings (+; *n* = 19) expressing *pmec-4::OSP-1* in the *osp-1(vd60)* background, and non-transgenic animals (-; *n* = 20) and transgenic siblings (+; *n* = 19) expressing *pmec-4::OSP-1* in the wt background. Comparisons between groups were done using one-way ANOVA with a Tukey's test for multiple comparisons. **e** Deconvolved spinning-disk confocal maximum projection of an ALM neuron of animals expressing the autophagy substrate reporter SQST-1::GFP under its endogenous promoter (*psqst-1::SQST-1::GFP*) in wt, *unc-51*, and non-transgenic animals (-) and transgenic siblings (+) expressing *pmec-4::OSP-1* in the *osp-1(vd60)* background. Scale bar 5 µm. **f** Quantification of the SQST-1 fluorescence in the ALM neurons of wt (*n* = 13), *unc-51* (*n* = 11), and non-transgenic animals (-; *n* = 14) and transgenic siblings (+; *n* = 11) expressing *pmec-4::OSP-1* in the *osp-1(vd60)* background. Comparisons between groups were done using the Krustal-Wallis test adjusted for multiple comparisons (Dunn's test). In panels (**d** and **f**) measures of center represent mean values, each dot represents an animal; error bars are SEM.

conditions with both chronic and acute ROS increase. However, no treatment is currently available to protect neurons from this insult. Most human data regarding oxidative stress-induced neurodegeneration come from post-mortem studies, as in vivo investigations are extremely challenging. Here, the combination of a tractable genetic system with the KillerRed optogenetic tool to temporally and spatially control ROS production, along with the development of the iBox to conduct a forward genetic screen in a time-efficient manner, were instrumental in the identification of *osp-1*, a previously uncharacterized molecule with neuroprotective functions. Using online modeling tools, we gained insight into several structural features of OSP-1, such as the presence of a transmembrane domain and the predicted structural domains, with homologs in the nematode phylum. RNA sequencing and tiling array analyses have revealed different conditions in which *osp-1*, amongst several other genes, is up- or down-regulated. One of these studies reported that *osp-1* is up-regulated in response to bacterial infection with *Enterococcus faecalis*[44]. Our results reveal that OSP-1 is expressed in six bilateral pairs of *C. elegans* neurons, including the ALM neurons, and that its expression is upregulated by acute oxidative stress. We also identified the importance of *osp-1* expression level, with the causative mutation *vd60* resulting in a loss-of-function due to reduced expression rather than a defect in protein function due to the glutamate to glycine substitution per se. This is corroborated by the fact that the mutated version of OSP-1 is a functional molecule that can rescue KillerRed-induced cell death.

Importantly, this study provides insight into the cell-autonomous function of OSP-1 in protecting neurons from oxidative stress insults, with its overexpression conferring protection against KillerRed-induced degeneration in mechanosensory neurons and 6-OHDA-dependent degeneration in dopaminergic neurons. Our work also demonstrates that heterologous OSP-1 is sufficient to rescue hypoxia-induced degeneration in rodent and human cells, revealing the existence of a common pathway.

Our results show that OSP-1 localizes to the ER, starting in early developmental stages. Mutations in *osp-1* reduce ER branching in the proximal segment of the axon and, conversely, its overexpression leads to a dramatic rearrangement and accumulation of the ER in that region. Axonal ER rearrangements have been reported in the context of regeneration following injury, and are believed to be the drivers of the regrowth process[82]. However, the phenotype of ER accumulation in the proximal axonal region is not well documented.

In our model, we demonstrate that animals with protective OSP-1 overexpression display not only ER rearrangement but also dispersion of lysosomes away from the cell body, with an increased number appearing in the neurite. Conversely, *osp-1* mutants display a greater presence of lysosomes in the cell body, with clustering occurring near the soma. Lysosomes are needed in the cell body to complete the degradative process in autophagy, and it has been shown that lysosomes cluster in the proximity of the cell body in response to nutrient depletion, which induces autophagy. In contrast, when nutrients are
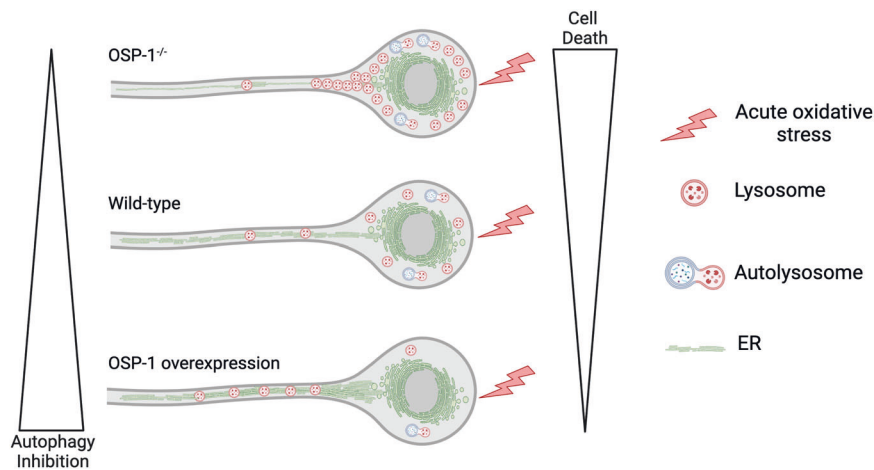
Fig. 10 | Model for OSP-1 neuroprotection against acute oxidative stress. We propose that OSP-1 functions at the ER as a negative regulator of autophagy. Mutations in OSP-1 (OSP-1$^{-/-}$; top section) lead to decreased ER branching in the axonal proximal segment and an increase of lysosomes in the cell body with clustering between the soma and the axon, which is associated with higher autophagy; this results in enhanced oxidative stress-induced autophagy-dependent cell death, compared to wild-type (middle section). In contrast, OSP-1 overexpression (bottom section) causes a rearrangement of the ER towards the proximal region of the axon, accompanied by a dispersion of lysosomes from the cell body towards the neurite, with consequent reduction of autophagy and reduced cell death. Created in BioRender. Ritchie, F. (2024) https://BioRender.com/d57p325.

abundant, autophagy is reduced, and lysosomes are dispersed towards the periphery[71]. Thus, our results suggest a link between OSP-1 mutation and lysosome clustering, increased degeneration, and a possibly higher autophagy state, whereas OSP-1 overexpression correlates with lysosome dispersion, neuroprotection, and a potentially lower autophagy state. These associations highlight potential roles for OSP-1 in lysosome positioning and autophagy modulation, though further studies are required to elucidate the underlying mechanisms.

Although autophagy induction upon starvation generally promotes cell survival, and its activation is thought to be beneficial in removing protein aggregates in neurodegenerative disorders[83,84], autophagy also mediates developmental programmed cell death and cellular degeneration under extreme stress conditions, through sustained consumption of cytoplasmic components and organellar demise[85,86]. Autophagy-dependent cell death, as defined by the Nomenclature Committee of Cell Death, is "a form of regulated cell death that mechanistically depends on the autophagic machinery (or components thereof)"[87], and that is independent of apoptosis or necrosis. This is distinct from autophagy-associated cell-death, where autophagy coincides with apoptosis or other cell-death pathways, and from autophagy-mediated cell-death in which autophagy triggers apoptosis[86]. Autophagy-dependent cell death has been well studied in *Drosophila melanogaster* as the process that mediates midgut degradation[88]. In *C. elegans*, autophagy participates in programmed cell death during development, when the apoptotic pathway is compromised, and is required in the germline for the degeneration induced by genotoxic stress[89]. In line with this notion, there is increasing evidence that the inhibition of autophagy results in better outcomes, particularly in certain classes of neurons with low basal autophagy (dopaminergic neurons), and in conditions of acute insults[90,91]. Our results are consistent with ROS inducing autophagy-dependent neuronal death, with OSP-1 being a negative regulator of this process. In fact, in our paradigm, we found a reduction in cell death in animals with mutations in the autophagy molecules UNC-51, ATG-13 and ATG-3, but no effect when the apoptotic or necrotic pathways were inhibited, suggesting that oxidative stress induces autophagy-dependent cell death. Our genetic results demonstrate that OSP-1 acts upstream of the initiator of autophagy UNC-51 and has an inhibitory role, with overexpression of OSP-1 resulting in a reduced level of autolysosomes and an increase in the autophagy substrate SQST-1, similar to the results obtained in animals with a mutation in

UNC-51. Although we observed a trend towards increased autolysosomes and reduced SQST-1::GFP in *osp-1* mutant animals, in line with a higher autophagy state, this did not reach statistical significance.

Our results show that mutation in *osp-1* reduces lifespan, and we propose that this effect is due to the role of OSP-1 as a negative regulator of autophagy. Our results are supported by work from Wilhelm and colleagues[92], who show that inactivation of the autophagy gene *bec-1*, specifically in neurons, extends lifespan. Moreover, recent work from the Kumsta and Hansen laboratories has demonstrated that neuronal-specific knock down of early-acting autophagy genes leads to extended lifespan through a mechanism independent from canonical autophagy[93]. However, contrary to these results, the reduction of autophagy in neurons driven by the age-dependent increased expression of the gene *rub-1* (Rubicon) leads to reduced lifespan[94]. It is possible that different autophagy genes have differing expression patterns, compensatory mechanisms or timing resulting in conflicting data that have not been addressed in this study.

Taken together, our results suggest that OSP-1 may function as a modulator of autophagy, potentially acting upstream of UNC-51. However, since our study did not specifically investigate autophagy flux, it remains to be determined whether OSP-1 impacts specific elements of this process or has different functions in other cellular contexts. Autophagy is a well-characterized process, and its regulators, which act through phosphorylation (e.g., mTORC1 and AMPK) and ubiquitination (e.g., several E3 ligases), are heavily involved in multiple cellular pathways[95]. Our study identifies OSP-1 as a potential regulator of autophagy with a neuroprotective function.

Methods
Strains and genetics
Standard techniques were used for *C. elegans* maintenance, crosses, and other genetic manipulations[96]. Animals were grown at 20 °C, on Nematode Growth Medium (NGM) plates seeded with *Escherichia coli* (*E. coli*), strain OP50. Experiments were performed at room temperature (22 °C). The wild-type strain N2 Bristol was used together with the KillerRed-integrated strain QH5898 *vdIs24[pmec-4::KillerRed; podr-1::dsRed]; zdIs5[pmec-4::GFP; lin-15(+)]*. This strain originated from the integration of the extra-chromosomal array *vdEx406[pmec-4::KillerRed (20 ng/µl); podr-1::dsRed (60 ng/µl)]* into the genome by treatment with trimethylpsoralen followed by ultraviolet irradiation (TMP-UV), and

subsequent outcrossing with the CZ10175 *zdIs5[pmec-4::GFP; lin-15(+)]* to remove background mutations. All other strains generated in this study are listed in Supplementary Tables 1–5. The following strains were obtained from the *Caenorhabditis* Genetic Center (CGC): CZ10175 *zdIs5[pmec-4::GFP; lin-15(+)] I*, TG2435 *vtIs1[pdat-1::GFP + rol-6(su1006)] V*, CB1189 *unc-51(e1189) V*, CB369 *unc-51(369) V*, CB1472 *mec-6(e1342) I*, MT1522 *ced-3(n717) IV*, HZ1688 *atg-13(bp414) III*, HZ1684 *atg-3(bp412) IV; him-5(e1490) V* and MAH349 *sqIs35[psqst-1::SQST-1::GFP; punc-122::RFP]*. The strains FX14768 *pas-6(tm1942)/nT1 V* and FX00858 *clp-1(tm858) III* were obtained from the National BioResources Project (NBRP): *C. elegans*. The strains TU3973 *uIs149[pmec-6::MEC-6::tagRFP]* and TU3969 *uIs144[pmec-4::YFP::PISY-1]* were a kind gift from Martin Chalfie, and the strains XMN959 *bggSi14[pmec-7::mCherry::GFP::LGG-1; prps-27::NeoR] II* and XMN1358 *bggSi20[pmec-7::UNC-51, prps-27::Neo]; muIs32[pmec-7::GFP, lin-15(+)] II* were kindly donated by Brock Grill. The strain containing the integrated transgene *jsIs1111[pmec-4::UNC-104::GFP]* was a kind gift from Michael Nonet. The strain PHX2500 carrying the *osp-1* allele *syb2500* was generated by SunyBiotech.

iBox illumination system
The iBox components are a power input (18 volts, 8 amps), a fuse (10 amps), an LM7812 regulator (12 volts, 1 amp), and a computer fan (80 mm, 12 volts). Each Green Rebel LED (530 nm) is attached to a SinkPAD-II (20 mm Tri-Star Base - 489 lm @ 700 mA) and has a heat sink (https://www.luxeonstar.com/40mm-square-7.9-degree-cw-alpha-heat-sink). The diode (200 volts, 1 amp) is used to isolate the 12 LED-driver circuits from each other, the capacitor (50 volts, 1000 microfarad) filters the noise on the power supply for each PowerPuck driver, and the resistor (10 hm, 3 watts) limits the capacitor charging current once the device is switched on.

KillerRed activation
Illumination with green light using a dissecting microscope was performed as previously described[29]. In brief, 20-30 well-fed animals at the last larval stage (L4 stage) were transferred to a non-seeded NGM plate, placed into a drop of 0.05% tetramisole hydrochloride (which functions as an anesthetic) to avoid dispersion, and illuminated for 30 min. Illumination using green 530 nm LEDs (3 LXMLPM01- 0100 Green LUXEON Rebel LED soldered to a SinkPAD-II™ 20 mm Tri-Star base) was performed on 20-30 well-fed L4 animals that were transferred to small unseeded plates from the cold room (2.5 °C). Animals were placed into a drop of 0.05% tetramisole hydrochloride and illuminated for 1 h. Anesthetized animals were restricted to a small area of the plate (~3 mm²) to avoid variation of light intensity. In both protocols, a drop of M9 buffer was delivered to the animals after illumination and *E. coli* was streaked onto the plate to allow the recovering animals to feed. Each experiment was repeated multiple times: typically, three experiments were conducted unless a sample size of ~100 ALM neurons (enough to reach statistical power) was obtained in two experiments. For transgenic strains carrying extrachromosomal DNA, the controls were provided by the non-transgenic siblings that were illuminated simultaneously as a mixed population of animals, selected and scored blindly (the presence or lack of the co-injection marker in the red channel was revealed after scoring the cell death in the green channel). In the case of mutant strains, from each genetic cross performed to introduce the desired mutation together with the KillerRed and *zdIs5* transgene (GFP in ALM neurons), we re-isolated a wild-type strain which we then tested side-by-side with the mutant strain of interest, to ensure a more uniform genetic background. Wild-type controls were included at each trial to confirm KillerRed activation.

Neuronal analysis
Cell death was quantified 24 h after illumination. Cells were scored as *dead* if they either completely disappeared or persisted as a sole cell body, without any residual neurite attached. Neurons were scored as *intact* if they presented an unaltered morphology, *short* if their process did not extend to the full length, and *damaged* if the neurite presented a break visible as an interruption of GFP continuity. Data were imported into Prism9 as the mean percentage of cell death, the standard error of proportion, and the total number of ALM neurons analyzed for any given genotype.

EMS protocol
Ethyl methanesulfonate (EMS) is a carcinogen, and all work was performed in a fume hood. Everything used during mutagenesis was decontaminated with NaOH (1 M) by immersion overnight before separate disposal of liquid and solid waste. L4 mutagenized animals were used for the highest efficiency. Animals were collected from an NGM plate containing a large population, predominantly at the L4 stage, using M9 buffer and transferred to a glass 15 ml tube (up to 2 ml); 20 μl of EMS were added to 2 ml of M9 buffer and mixed into solution (50 mM final concentration). The 2 ml of animals were then added to the EMS solution. The tube was sealed with parafilm and agitated every 30 min over a 4-hour incubation period, after which as much of the EMS solution possible was removed and animals were washed three times with ~15 ml of M9 buffer, allowing them to settle by gravity between wash steps. After the final wash, the animals were transferred with a small volume of M9 buffer to an OP50-seeded NGM plate and allowed to dry without the lid in the fume hood. Once the M9 buffer had dried, the plate was closed, and the animals were allowed to recover for ~1 h (the plate was left in the fume hood for the recovery period to allow any residual EMS to evaporate). 50 P0 animals were cloned on 30 OP50-seeded NGM plates. About 20 F1 animals from each of the 30 P0 plates were cloned and the progeny (F2s) of ~400 F1s were analyzed for mutations. F2 populations containing mutant animals with significantly altered cell death would shift the wild-type cell-death levels (~50%) higher or lower as they would contribute to 25% of the phenotype for recessive mutations and 75% for dominant mutations. Mutant animals were cloned, and their progeny were analyzed to ensure that the phenotypes had bred true. The data presented in Fig. 1d are relative to the *vd60* strain that was outcrossed four times (4X) with the N2 wild-type strain, to remove other possible EMS mutations from the background. Given that, similar to hermaphrodites, *vd60* males also have an increased cell death in ALM neurons compared to wild-type animals (Supplementary Fig. 2a), heterozygous F1 males from the cross between *vd60* hermaphrodites and wild-type males were tested to see if the mutation was recessive. The animals (*vd60/+*) presented the same level of ALM cell death as wild-type animals, indicating that the *vd60* mutation is recessive (Supplementary Fig. 2b). It is worth noting that OSP-1 expression is greater in males compared to hermaphrodites possibly explaining the milder KillerRed-induced neurodegeneration observed in *osp-1(vd60)* mutant males.

Full genome sequencing data analysis
After removing adapter sequences (software BBMap, version 37.31, quality filter of 10, and minimum length of 25 bp) the output sequences were aligned to the *C. elegans* genome (ce10) (software BBMap). The output of alignment was sorted by position and duplicated reads were removed. Gene variant calling was performed (software FreeBayes with default settings: if read depth was less than 2 it was filtered out from output of variant calling) and the background variants (variants in N2 and KillerRed strain) were deducted from variants of each sample (*vd60*). Finally, variants were annotated (software Annovar)[97].

Genome mapping
The *vd60* mutation was mapped as previously described[39,40]. Briefly, after several rounds of outcrosses, most of the EMS mutations (typically G to A and C to T substitutions) that are far away from the causal mutation (*vd60*) will be lost; in contrast, mutations linked to the causal mutations will remain in a discrete region along one of the six

chromosomes as they are less likely to recombine due to the close proximity to the mutation of interest selected during the outcrosses. Plotting the number of these typical EMS substitutions for each Megabase (Mb) of each chromosome allows them to be mapped to those physical regions where the causal mutation is more likely to be found. Following EMS mapping, every gene on the 8th Mb of Chromosome I (the peak with the highest number of mutations for the *vd60* mutant animals) that contained exonic non-synonymous mutations was tested for causality by providing the wild-type copy of each of these genes under their endogenous promoters. This method allowed to determine that none of the genes except T28B8.6 (*osp-1*) conferred rescue or mimicked the *vd60* mutant phenotype (Supplementary Table 5).

Molecular biology, single-copy insertions, and CRIPSR-Cas9 gene editing

All constructs were generated using standard cloning[98], or Gibson assembly[99], with details of their construction being listed in Supplementary Tables 6–9.

The plasmid pSM was used as an empty vector in the injection mix (up to 100 ng). The plasmid 197 *plin-44::ChFP* was used as a co-injection marker (10-15 ng/µl). The plasmids 478 pSM *pmec-4*, 280 pSM *pmyo-3*, 281 pSM *pdpy-7*, 471 *pdat-1::UNC-71* were used as backbones for cell/tissue-specific expression of T28B8.6, mCherry, and SEL-11. The plasmid 332 *pmec-4::GFPnovo* was used as a backbone to generate the tag version of OSP-1, and the plasmid pDD284 Addgene (Goldstein lab) was used for the amplification and cloning of the tagRFP molecule with a linker sequence at the N-terminus used to fluorescently tag PAS-6.

For the rescue and/or overexpression of OSP-1 and UNC-51, PCR fragments of wild-type copies of these genes under their endogenous promoter and with their 3'UTR were generated using genomic DNA (for reagents see Supplementary Table 8).

MiniMos NeoR vectors were constructed using Gibson assembly of two PCR fragments to insert the construct of interest into the miniMos NeoR (pCFJ910 was a gift from Erik Jorgensen; Addgene plasmid #44481). Single-copy insertions were generated by injecting young adult animals with miniMos-based vectors at 10 ng/µl together with pGH8 10 ng/µl, pCFJ90 2.5 ng/µl, pCFJ104 10 ng/µl, pCFJ601 50 ng/µl, and pMA122 10 ng/µl (gifts from Erik Jorgensen; Addgene #34874 and #34873). Injected animals were transferred to OP50 plates (three per plate) and allowed to generate progeny at 25 °C. One day later, 500 µl of 25 mg/ml G418 was added to each plate for NeoR selection (Thermo Fisher Scientific). Plates were left to starve at 25 °C, and once starved were heat-shocked at 34 °C in an air incubator to kill animals carrying extra-chromosomal arrays. Four hours after heat shock, plates containing animals that were alive, lacked co-injection markers, and moved well, were transferred onto a fresh OP50 plate and grown at 20 °C. Two days later, single, healthy animals containing successful insertions were selected and placed into individual OP50 plates.

C. elegans CRISPR-Cas9 genome edits (*osp-1(vd98)*, *osp-1(vd99)*, *osp-1(vd84)*, *osp-1(vd2280)* and *osp-1(vd230)*) were generated as previously described[100]. In brief, edits were generated by gonadal microinjection of CRISPR-Cas9 protein complexes using *dpy-10* in a co-CRISPR strategy. Injections were performed using standard methods[101]. For *vd98*, *vd99*, *vd228* and *vd229* alleles, edits were conducted in the reference KillerRed strain (QH5898). For the *vd84* allele, edits were conducted in the wild-type N2 strain. All CRISPR reagents are listed in Supplementary Table 9. Guide RNAs were synthesized as Alt-R® CRISPR-Cas9 crRNA, 2 nmol (Integrated DNA Technologies). Injected animals were transferred to OP50 plates (two-three per plate) and allowed to generate progeny for 4 days at 20 °C. Efficient injection plates were identified by *dpy-10(cn64)* phenotypes (rollers heterozygous, dumpy homozygous). ~50–60 animals (roller or wild-type) were cloned from the best plates and genotyped via PCR for deletion

after 3 days. Candidate correct edits were cloned to obtain homozygous and remove any heterozygous *dpy-10* edits. Final strains were confirmed via Sanger sequencing and outcrossed three times.

Mammalian cell culture and hypoxia treatment

Rat pheochromocytoma PC12 cells (ATCC-CRL-1721, ATCC) were seeded onto 10 mm coverslips, double-coated with 0.0015% poly-L-ornithine (Sigma) (16–24 h) followed by 10 µg/ml laminin (Sigma) (3–16 h). PC12 cells were grown at 37 °C, 5% CO_2 on RPMI-1640 medium (Gibco-ThermoFisher) containing 10% horse serum (Gibco-ThermoFisher) and 5% fetal bovine serum (FBS) (Gibco-ThermoFisher). After 48 h, the cells were transfected using Lipofectamine 3000 (Gibco-ThermoFisher) as per the manufacturer's protocol. 24 h after transfection, cells were differentiated for 3–5 days using RPMI-1640 with 1% horse serum supplemented with 50 ng/ml nerve growth factor (STEMCELL Technologies).

Human neuroblastoma SH-SY5Y cells (94030304-1VL, Merck-Sigma-Aldrich) were seeded onto 10 mm coverslips, coated with 10 µg/ml laminin (Sigma) (3-16 h). The cells were grown at 37 °C, 5% CO_2 on DMEM/F12 medium (1:1) (Gibco-ThermoFisher) containing 15% FBS, 1x GlutaMAX (Gibco-ThermoFisher) and 1x Penicillin/Streptomycin (Gibco-ThermoFisher). After 24 h, the cells were transfected using Lipofectamine 3000 (Gibco-ThermoFisher) as per the manufacturer's protocol. 24 h after transfection, cells were differentiated by incubating for 3 days in DMEM/F12 (1:1) containing 1.5% FBS, 1x GlutaMAX, 1x Penicillin/Streptomycin and 10 µM all-*trans*-retinoic acid (RA) (Tocris), followed by 3 additional days in DMEM/F12 (1:1) containing 0.5% FBS, 1x GlutaMAX, 1x Penicillin/Streptomycin and 10 µM RA, and 3 days in neurobasal-A (Gibco-ThermoFisher) containing 1x GlutaMAX, 1x Penicillin/Streptomycin, 10 µM RA, 1x B27 (Gibco-ThermoFisher) and 50 ng/ml BDNF (STEMCELL Technologies).

Differentiated PC12 and SH-SY5Y cells were placed into a hypoxic chamber flushed with <1% oxygen and 5% CO_2 for 24 h. After treatment, cells were fixed with 4% paraformaldehyde for 15 min, washed repeatedly with phosphate-buffered saline (PBS), permeabilized with 0.01% Triton-X-100 in PBS for 10 min, and stained with DAPI for pyknotic nuclei count in YFP/GFP-positive cells.

PC12 cells (https://www.atcc.org/products/crl-1721) and SH-SY5Y cells (https://www.sigmaaldrich.com/AU/en/product/sigma/cb_94030304?srsltid=AfmBOoprJ4Q8kyunN-FPtOj959pY0RX5G8iPp1bbwNwy27_omcMwmbLw) were authenticated by the manufacturers.

DiI staining

The lipophilic DiI dye fluoresces red and stains six amphid cells in the head (ASK, ADL, ASI, AWB, ASH, ASJ) and two phasmid cells in the tail (PHA, PHB) of *C. elegans*. In brief, stock solutions of DiI were prepared in dimethyl formamide (DMF) at 2 mg/ml and stored protected from light at −20 °C. The stock was diluted 1 in 200 with M9 buffer. Individual animals (L4 stage) were incubated in a drop of DiI solution on a glass slide for 1.5 h at room temperature. After the incubation, animals were transferred to the unseeded section of an NGM plate seeded with OP50 to ensure that they crawled away from the DiI staining solution and fed on the bacteria to expel the dye from their intestine. After 30–60 min, the cells were visualized via fluorescence microscopy.

Microscopy

Animals were immobilized using 0.05% tetramisole hydrochloride on 3% agar pads. Observations were made with a Zeiss Axio Imager Z1 microscope equipped with a Photometrics Cool Snap HQ2 camera using Metamorph software. For the OSP-1/MEC-6 co-localization experiment, animals were immobilized with 0.05% tetramisole hydrochloride and visualized by mounting them on 4% agar pads after anesthesia, except for the LGG-1 analysis where sodium azide (25 mM) was used as anesthetic. Typically, animals at the L4 stage were imaged,

unless otherwise specified. *N* values for all *C. elegans* strains imaged are in the figure legends and/or Supplementary Table 4.

Imaging was performed at the Queensland Brain Institute's Advanced Microscopy Facility using a spinning disk confocal microscope (Marianas, Intelligent Imaging Innovations) equipped with a confocal scanner unit (CSU-W1, Yokogawa Electric Co.) built around an Axio Observer body (Z1, Carl Zeiss AG), and fitted with an sCMOS camera (ORCA-Flash4.0 V2, Hamamatsu Photonics) and SlideBook v6.0 software (3i) using a 100 × /1.3 NA oil-immersion objective with sampling intervals x, y = 63 nm and z = 160 nm. Images were deconvolved with Huygens Professional v19.10 run on a GPU-accelerated computer (3x NVIDIA® Tesla® V100) using the CMLE algorithm, with a signal to noise ratio of 20, background of 100, and 40 iterations. Images exported in ICS2 format. In Fig. 6a, image acquisition was performed using a Zeiss C Plan-Apochromat 63x/1.4 NA oil-immersion objective on a confocal/two-photon laser-scanning microscope (LSM 980 NLO Airyscan 2, Carl Zeiss GmbH) built around an Axio Observer 7 body and equipped with an Airyscan 2 super-resolution detector, a 34-channel spectral photomultiplier tube (PMT) array, two internal GaAsP PMTs, a transmission PMT, and two external GaAsP PMTs for non-descanned detection in two-photon microscopy, and controlled by Zen Blue software. Images were deconvolved using the Airyscan Joint Deconvolution (10 iterations).

Colocalization was determined by selecting a 15 μm region of interest (ROI) square around a z-stack (rotated so that the dorsal was up and anterior was on the left) of the whole ALM cell body of deconvolved images in ImageJ v1.52r, saved as single channels before importing to the colocalization analyzer wizard in Huygens Professional v19.10, with the estimation threshold setting selected as 'none' to determine the Pearson's *R*-Value. Measurements of PAS-6 and LGG-1 puncta, lysosomes, ER proximal branching and accumulation, and SQST-1 fluorescence were conducted with ImageJ.

Light touch assay
This assay was conducted to determine whether animals were responsive to light mechanical stimuli and was performed with an eyebrow attached to a pipette tip. In wild-type animals, a gentle touch on the tail of the animal elicited a forward movement, whereas a touch on the head elicited a backward movement. Adult animals were individually transferred to small unseeded plates to allow the analysis of individual animals' behavior. After a 5 min resting period, each animal was assayed 10 times, alternating head and tail gentle touches. For each animal, positive responses were calculated as the percentage of the total number of gentle touches. The result of the assay for each genotype is presented as the average positive response for the total number of animals assayed[102].

Lifespan assay
The assays were performed based on previous protocols[48]. In brief, several animals at the L4 stage were placed into small NGM plates freshly seeded with OP50 and moved to new plates every few days to avoid mixing with the progeny. Animals were checked every day, and dead animals (that did not respond to harsh touch with a platinum wire) were removed. Animals with internally hatched larvae (bag of worms) and burst animals were excluded from the assay. Lifespan curves were generated using OASIS (Online application for Survival Analysis) http://sbi.postech.ac.kr/oasis/. The experiments were repeated three times.

6-OHDA assay
The assays were performed based on previous protocols[48], with some modifications. In brief, adult animals (~ 10) were incubated at room temperature (22 °C) in 60 μl of M9 without food on a shaker rotating at 17 rpm for 24 h. The next day, solutions of ascorbic acid (200 mM) and 6-OHDA (125 mM) were freshly prepared in water and added to the 60 μl of M9 now containing L1 larvae (the final concentration of 6-OHDA was 25 mM). After 1.5 h of incubation at room temperature and rotating at 17 rpm, 300 μl M9 buffer was added to oxidize and inactivate the 6-OHDA. The animals were pipetted to one half of an NGM plate containing a stripe of OP50 bacteria on the opposite half of the plate, and adult animals and eggs were picked off to prevent the growth of those that were not treated at the L1 stage. Plates were incubated at 20 °C for two days before examining the effects of the treatment with 6-OHDA. The experiments were conducted in three technical replicates.

Statistical analysis
Statistical analyses were performed using Prism9 unless otherwise specified. Two-tailed unpaired t-tests (parametric) or Mann-Whitney tests (non-parametric) were used to compare two populations. One-way ANOVA with a Tukey's test for multiple comparisons (parametric) or the Kruskal-Wallis tests adjusted for multiple comparisons using a Dunn's test (non-parametric) were the statistical tests of choice when the analysis contained more than two populations. Two-way ANOVA adjusted for multiple comparisons was used to compare the proportions of different phenotypes across multiple conditions. All exact p-values can be found in the Source Data file.

Bioinformatics analysis
The open reading frame and exon-intron structure of *T28B8.6* were derived from information compiled in WormBase. Protein domains, signal peptide, and topology were predicted with InterPro, Phobius, TMHMM v. 2.0, and HMMTOP. Structural prediction was done with AlphaFold2[103,104].

Reporting summary
Further information on research design is available in the Nature Portfolio Reporting Summary linked to this article.

Data availability
The datasets generated and analyzed for Figs. 1–9 and Supplementary Figs. 2–12 are provided in the Source Data file. Source data are provided with this paper.

References
1. Tauffenberger, A. & Magistretti, P. J. Reactive oxygen species: beyond their reactive behavior. *Neurochem. Res.* **46**, 77–87 (2021).
2. Sies, H. & Jones, D. P. Reactive oxygen species (ROS) as pleiotropic physiological signalling agents. *Nat. Rev. Mol. Cell Biol.* **21**, 363–383 (2020).
3. Shadfar, S., Parakh, S., Jamali, M. S. & Atkin, J. D. Redox dysregulation as a driver for DNA damage and its relationship to neurodegenerative diseases. *Transl. Neurodegener.* **12**, 18 (2023).
4. Singh, A. et al. Lipid mediated brain disorders: a perspective. *Prostaglandins Other Lipid Mediat*, **167**, 106737 (2023).
5. Salim, S. Oxidative stress and the central nervous system. *J. Pharm. Exp. Ther.* **360**, 201–205 (2017).
6. Mecocci, P., MacGarvey, U. & Beal, M. F. Oxidative damage to mitochondrial DNA is increased in Alzheimer's disease. *Ann. Neurol.* **36**, 747–751 (1994).
7. Ferrante, R. J. et al. Evidence of increased oxidative damage in both sporadic and familial amyotrophic lateral sclerosis. *J. Neurochem* **69**, 2064–2074 (1997).
8. Alam, Z. I. et al. Oxidative DNA damage in the Parkinsonian brain: an apparent selective increase in 8-hydroxyguanine levels in substantia nigra. *J. Neurochem* **69**, 1196–1203 (1997).
9. Browne, S. E. et al. Oxidative damage and metabolic dysfunction in Huntington's disease: selective vulnerability of the basal ganglia. *Ann. Neurol.* **41**, 646–653 (1997).

10. Wang, J., Xiong, S., Xie, C., Markesbery, W. R. & Lovell, M. A. Increased oxidative damage in nuclear and mitochondrial DNA in Alzheimer's disease. *J. Neurochem* **93**, 953–962 (2005).

11. Schulz, J. B. & Beal, M. F. Mitochondrial dysfunction in movement disorders. *Curr. Opin. Neurol.* **7**, 333–339 (1994).

12. Giasson, B. I. et al. Oxidative damage linked to neurodegeneration by selective alpha-synuclein nitration in synucleinopathy lesions. *Science* **290**, 985–989 (2000).

13. Machiela, E., Dues, D. J., Senchuk, M. M. & Van Raamsdonk, J. M. Oxidative stress is increased in *C. elegans* models of Huntington's disease but does not contribute to polyglutamine toxicity phenotypes. *Neurobiol. Dis.* **96**, 1–11 (2016).

14. Xie, H. et al. Rapid cell death is preceded by amyloid plaque-mediated oxidative stress. *Proc. Natl Acad. Sci. USA* **110**, 7904–7909 (2013).

15. Love, S. Oxidative stress in brain ischemia. *Brain Pathol.* **9**, 119–131 (1999).

16. Manzanero, S., Santro, T. & Arumugam, T. V. Neuronal oxidative stress in acute ischemic stroke: sources and contribution to cell injury. *Neurochem Int* **62**, 712–718 (2013).

17. George, P. M. & Steinberg, G. K. Novel Stroke Therapeutics: Unraveling stroke pathophysiology and its impact on clinical treatments. *Neuron* **87**, 297–309 (2015).

18. Amberg, G. C., Earley, S. & Glapa, S. A. Local regulation of arterial L-type calcium channels by reactive oxygen species. *Circ. Res* **107**, 1002–1010 (2010).

19. Bundy, R. E. et al. Redox regulation of p38 MAPK activation and expression of ICAM-1 and heme oxygenase-1 in human alveolar epithelial (A549) cells. *Antioxid. Redox Signal* **7**, 14–24 (2005).

20. Martinez-Reyes, I. & Cuezva, J. M. TheH. The H(+)-ATP synthase: a gate to ROS-mediated cell death or cell survival. *Biochim. Biophys. Acta.* **1837**, 1099–112 (2014).

21. Ray, P. D., Huang, B. W. & Tsuji, Y. Reactive oxygen species (ROS) homeostasis and redox regulation in cellular signaling. *Cell Signal* **24**, 981–990 (2012).

22. Gao, Y. et al. New insights into the interplay between autophagy and oxidative and endoplasmic reticulum stress in neuronal cell death and survival. *Front Cell Dev. Biol.* **10**, 994037 (2022).

23. Bulina, M. E. et al. A genetically encoded photosensitizer. *Nat. Biotechnol.* **24**, 95–99 (2006).

24. Carpentier, P., Violot, S., Blanchoin, L. & Bourgeois, D. Structural basis for the phototoxicity of the fluorescent protein KillerRed. *FEBS Lett.* **583**, 2839–2842 (2009).

25. Pletnev, S. et al. Structural basis for phototoxicity of the genetically encoded photosensitizer KillerRed. *J. Biol. Chem.* **284**, 32028–32039 (2009).

26. Roy, A., Carpentier, P., Bourgeois, D. & Field, M. Diffusion pathways of oxygen species in the phototoxic fluorescent protein KillerRed. *Photochem Photobio. Sci.* **9**, 1342–1350 (2010).

27. Serebrovskaya, E. O. et al. Targeting cancer cells by using an antireceptor antibody-photosensitizer fusion protein. *Proc. Natl Acad. Sci. USA* **106**, 9221–9225 (2009).

28. Teh, C. et al. Optogenetic in vivo cell manipulation in KillerRed-expressing zebrafish transgenics. *BMC Developmental Biol.* **10**, 110 (2010).

29. Williams, D. C. et al. Rapid and permanent neuronal inactivation in vivo via subcellular generation of reactive oxygen with the use of KillerRed. *Cell Rep.* **5**, 553–563 (2013).

30. Chalfie, M. & Au, M. Genetic control of differentiation of the *Caenorhabditis elegans* touch receptor neurons. *Science* **243**, 1027–1033 (1989).

31. Chalfie, M. & Sulston, J. Developmental genetics of the mechanosensory neurons of *Caenorhabditis elegans*. *Dev. Biol.* **82**, 358–370 (1981).

32. Gallegos, M. E. & Bargmann, C. I. Mechanosensory neurite termination and tiling depend on SAX-2 and the SAX-1 kinase. *Neuron* **44**, 239–249 (2004).

33. Hilliard, M. A. & Bargmann, C. I. Wnt signals and frizzled activity orient anterior-posterior axon outgrowth in *C. elegans*. *Dev. Cell* **10**, 379–390 (2006).

34. Neumann, B. & Hilliard, M. A. Loss of MEC-17 leads to microtubule instability and axonal degeneration. *Cell Rep.* **6**, 93–103 (2014).

35. Neumann, B., Nguyen, K. C. Q., Hall, D. H., Ben-Yakar, A. & Hilliard, M. A. Axonal regeneration proceeds through specific axonal fusion in transected *C. elegans* neurons. *Dev. Dynam* **240**, 1365–1372 (2011).

36. Syntichaki, P. & Tavernarakis, N. Genetic models of mechanotransduction: the nematode *Caenorhabditis elegans*. *Physiol. Rev.* **84**, 1097–1153 (2004).

37. White, J. G., Southgate, E., Thomson, J. N. & Brenner, S. The structure of the nervous-system of the nematode *Caenorhabditis elegans*. *Philos. T R. Soc. B* **314**, 1–340 (1986).

38. Zhang, Y. et al. Identification of genes expressed in *C. elegans* touch receptor neurons. *Nature* **418**, 331–335 (2002).

39. Zuryn, S., Le Gras, S., Jamet, K. & Jarriault, S. A strategy for direct mapping and identification of mutations by whole-genome sequencing. *Genetics* **186**, 427–430 (2010).

40. Zuryn, S. & Jarriault, S. Deep sequencing strategies for mapping and identifying mutations from genetic screens. *Worm* **2**, e25081 (2013).

41. Lionaki, E. & Tavernarakis, N. Oxidative stress and mitochondrial protein quality control in aging. *J. Proteom.* **92**, 181–194 (2013).

42. Stenico, M., Lloyd, A. T. & Sharp, P. M. Codon usage in *Caenorhabditis elegans*: delineation of translational selection and mutational biases. *Nucleic Acids Res* **22**, 2437–2446 (1994).

43. Sharp P.M., a. B. K. R. in *C. elegans II. 2nd Edition.* (ed Blumenthal T. Riddle D.L., Meyer B.J., et al., editors.) (Cold Spring Harbor Laboratory Press., Cold Spring Harbor (NY), 1997).

44. Engelmann, I. et al. A comprehensive analysis of gene expression changes provoked by bacterial and fungal infection in *C. elegans*. *PLoS One* **6**, e19055 (2011).

45. Yang, W. et al. Overlapping and unique signatures in the proteomic and transcriptomic responses of the nematode *Caenorhabditis elegans* toward pathogenic Bacillus thuringiensis. *Dev. Comp. Immunol.* **51**, 1–9 (2015).

46. Zhang, A. et al. Potential genetic damage to nematode offspring following exposure to triclosan during pregnancy. *Mol. Med Rep.* **16**, 1321–1327 (2017).

47. Cooper, J. F. & Van Raamsdonk, J. M. Modeling Parkinson's disease in *C. elegans*. *J. Parkinsons Dis.* **8**, 17–32 (2018).

48. Offenburger, S. L. et al. 6-OHDA-induced dopaminergic neuro-degeneration in *Caenorhabditis elegans* is promoted by the engulfment pathway and inhibited by the transthyretin-related protein TTR-33. *PLoS Genet* **14**, e1007125 (2018).

49. Nass, R. & Blakely, R. D. The *Caenorhabditis elegans* dopaminergic system: opportunities for insights into dopamine transport and neurodegeneration. *Annu Rev. Pharm. Toxicol.* **43**, 521–544 (2003).

50. Nass, R., Hall, D. H., Miller, D. M. 3rd & Blakely, R. D. Neurotoxin-induced degeneration of dopamine neurons in *Caenorhabditis elegans*. *Proc. Natl Acad. Sci. USA* **99**, 3264–3269 (2002).

51. Maulik, M., Mitra, S., Bult-Ito, A., Taylor, B. E. & Vayndorf, E. M. Behavioral phenotyping and pathological indicators of Parkinson's disease in *C. elegans* Models. *Front Genet* **8**, 77 (2017).

52. Masoudi, N., Ibanez-Cruceyra, P., Offenburger, S. L., Holmes, A. & Gartner, A. Tetraspanin (TSP-17) protects dopaminergic neurons against 6-OHDA-induced neurodegeneration in C. elegans. *PLoS Genet* **10**, e1004767 (2014).

53. Nass, R., Miller, D. M. & Blakely, R. D. *C. elegans*: a novel pharmacogenetic model to study Parkinson's disease. *Parkinsonism Relat. Disord.* **7**, 185–191 (2001).

54. Cao, Z. et al. Thirty-five percent oxygen pre-conditioning protects PC12 cells against death induced by hypoxia. *Free Radic. Res* **43**, 58–67 (2009).

55. Chen, Y. et al. *Caenorhabditis elegans* paraoxonase-like proteins control the functional expression of DEG/ENaC mechanosensory proteins. *Mol. Biol. Cell* **27**, 1272–1285 (2016).

56. Kumar, J. et al. The *Caenorhabditis elegans* Kinesin-3 motor UNC-104/KIF1A is degraded upon loss of specific binding to cargo. *PLoS Genet* **6**, e1001200 (2010).

57. Schwarz, D. S. & Blower, M. D. The endoplasmic reticulum: structure, function and response to cellular signaling. *Cell Mol. Life Sci.* **73**, 79–94 (2016).

58. Corazzari, M., Gagliardi, M., Fimia, G. M. & Piacentini, M. Endoplasmic reticulum stress, unfolded protein response, and cancer cell fate. *Front Oncol.* **7**, 78 (2017).

59. Yamamoto, Y. H. & Noda, T. Autophagosome formation in relation to the endoplasmic reticulum. *J. Biomed. Sci.* **27**, 97 (2020).

60. Albert, S. et al. Direct visualization of degradation microcompartments at the ER membrane. *P Natl Acad. Sci. USA* **117**, 1069–1080 (2020).

61. Raynes, R., Pomatto, L. C. & Davies, K. J. Degradation of oxidized proteins by the proteasome: distinguishing between the 20S, 26S, and immunoproteasome proteolytic pathways. *Mol. Asp. Med* **50**, 41–55 (2016).

62. Tanaka, K. The proteasome: overview of structure and functions. *Proc. Jpn Acad. Ser. B Phys. Biol. Sci.* **85**, 12–36 (2009).

63. Budenholzer, L., Cheng, C. L., Li, Y. & Hochstrasser, M. Proteasome structure and assembly. *J. Mol. Biol.* **429**, 3500–3524 (2017).

64. Zhang, L., Sheng, R. & Qin, Z. The lysosome and neurodegenerative diseases. *Acta Biochim Biophys. Sin. (Shanghai)* **41**, 437–445 (2009).

65. Koh, J. Y., Kim, H. N., Hwang, J. J., Kim, Y. H. & Park, S. E. Lysosomal dysfunction in proteinopathic neurodegenerative disorders: possible therapeutic roles of cAMP and zinc. *Mol. Brain* **12**, 18 (2019).

66. Lie, P. P. Y. & Nixon, R. A. Lysosome trafficking and signaling in health and neurodegenerative diseases. *Neurobiol. Dis.* **122**, 94–105 (2019).

67. Ballabio, A. & Gieselmann, V. Lysosomal disorders: from storage to cellular damage. *Biochim Biophys. Acta* **1793**, 684–696 (2009).

68. Edwards, S. L. et al. An organelle gatekeeper function for *Caenorhabditis elegans* UNC-16 (JIP3) at the axon initial segment. *Genetics* **194**, 143–161 (2013).

69. Ferguson, S. M. Neuronal lysosomes. *Neurosci. Lett.* **697**, 1–9 (2019).

70. Cai, Q. et al. Snapin-regulated late endosomal transport is critical for efficient autophagy-lysosomal function in neurons. *Neuron* **68**, 73–86 (2010).

71. Korolchuk, V. I. et al. Lysosomal positioning coordinates cellular nutrient responses. *Nat. Cell Biol.* **13**, 453–460 (2011).

72. Matsuura, A., Tsukada, M., Wada, Y. & Ohsumi, Y. Apg1p, a novel protein kinase required for the autophagic process in *Saccharomyces cerevisiae*. *Gene* **192**, 245–250 (1997).

73. Crawley, O. et al. Autophagy is inhibited by ubiquitin ligase activity in the nervous system. *Nat. Commun.* **10**, 5017 (2019).

74. Ogura, K. et al. *Caenorhabditis elegans unc-51* gene required for axonal elongation encodes a novel serine/threonine kinase. *Genes Dev.* **8**, 2389–2400 (1994).

75. McIntire, S. L., Garriga, G., White, J., Jacobson, D. & Horvitz, H. R. Genes necessary for directed axonal elongation or fasciculation in *C. elegans*. *Neuron* **8**, 307–322 (1992).

76. Hedgecock, E. M., Culotti, J. G., Thomson, J. N. & Perkins, L. A. Axonal guidance mutants of *Caenorhabditis elegans* identified by filling sensory neurons with fluorescein dyes. *Dev. Biol.* **111**, 158–170 (1985).

77. Melendez, A. & Levine, B. Autophagy in *C. elegans*. *WormBook*, 1–26 https://doi.org/10.1895/wormbook.1.147.1 (2009).

78. Fang, D., Xie, H., Hu, T., Shan, H. & Li, M. Binding Features and Functions of ATG3. *Front Cell Dev. Biol.* **9**, 685625 (2021).

79. Syntichaki, P., Xu, K., Driscoll, M. & Tavernarakis, N. Specific aspartyl and calpain proteases are required for neurodegeneration in *C. elegans*. *Nature* **419**, 939–944 (2002).

80. Zhang, H. et al. Guidelines for monitoring autophagy in *Caenorhabditis elegans*. *Autophagy* **11**, 9–27 (2015).

81. Kumsta, C. et al. The autophagy receptor p62/SQST-1 promotes proteostasis and longevity in *C. elegans* by inducing autophagy. *Nat. Commun.* **10**, 5648 (2019).

82. Rao, K. et al. Spastin, atlastin, and ER relocalization are involved in axon but not dendrite regeneration. *Mol. Biol. Cell* **27**, 3245–3256 (2016).

83. Stavoe, A. K. H. & Holzbaur, E. L. F. Autophagy in Neurons. *Annu Rev. Cell Dev. Biol.* **35**, 477–500 (2019).

84. Cai, Q. & Ganesan, D. Regulation of neuronal autophagy and the implications in neurodegenerative diseases. *Neurobiol. Dis.* **162**, 105582 (2022).

85. Liu, Y. & Levine, B. Autosis and autophagic cell death: the dark side of autophagy. *Cell Death Differ.* **22**, 367–376 (2015).

86. Denton, D. & Kumar, S. Autophagy-dependent cell death. *Cell Death Differ.* **26**, 605–616 (2019).

87. Galluzzi, L. et al. Molecular mechanisms of cell death: recommendations of the nomenclature committee on cell death 2018. *Cell Death Differ.* **25**, 486–541 (2018).

88. Xu, T., Nicolson, S., Denton, D. & Kumar, S. Distinct requirements of Autophagy-related genes in programmed cell death. *Cell Death Differ.* **22**, 1792–1802 (2015).

89. Wang, H., Lu, Q., Cheng, S., Wang, X. & Zhang, H. Autophagy activity contributes to programmed cell death in *Caenorhabditis elegans*. *Autophagy* **9**, 1975–1982 (2013).

90. Hu, Z., Yang, B., Mo, X. & Xiao, H. Mechanism and regulation of autophagy and Its role in neuronal diseases. *Mol. Neurobiol.* **52**, 1190–1209 (2015).

91. Klionsky, D. J. et al. Autophagy in major human diseases. *EMBO J.* **40**, e108863 (2021).

92. Wilhelm, T. et al. Neuronal inhibition of the autophagy nucleation complex extends life span in post-reproductive C. elegans. *Genes Dev.* **31**, 1561–1572 (2017).

93. Yang, Y. et al. Autophagy protein ATG-16.2 and its WD40 domain mediate the beneficial effects of inhibiting early-acting autophagy genes in *C. elegans* neurons. *Nat. Aging* **4**, 198–212 (2024).

94. Nakamura, S. et al. Suppression of autophagic activity by Rubicon is a signature of aging. *Nat. Commun.* **10**, 847 (2019).

95. Jia, R. & Bonifacino, J. S. Negative regulation of autophagy by UBA6-BIRC6-mediated ubiquitination of LC3. *Elife* **8**, https://doi.org/10.7554/eLife.50034 (2019).

96. Brenner, S. The genetics of *Caenorhabditis elegans*. *Genetics* **77**, 71–94 (1974).

97. Smith, H. E. & Yun, S. Evaluating alignment and variant-calling software for mutation identification in *C. elegans* by whole-genome sequencing. *PLoS One* **12**, e0174446 (2017).

98. Sambrook, J., Russell, D. W. & Sambrook, J. *The condensed protocols from Molecular cloning: a laboratory manual*. (Cold Spring Harbor Laboratory Press, 2006).

99. Gibson, D. G. et al. Enzymatic assembly of DNA molecules up to several hundred kilobases. *Nat. Methods* **6**, 343–345 (2009).

100. McDonald, N. A., Fetter, R. D. & Shen, K. Assembly of synaptic active zones requires phase separation of scaffold molecules. *Nature* https://doi.org/10.1038/s41586-020-2942-0 (2020).

101. Mello, C. C., Kramer, J. M., Stinchcomb, D. & Ambros, V. Efficient gene transfer in C.elegans: extrachromosomal maintenance and

integration of transforming sequences. *EMBO J.* **10**, 3959–3970 (1991).

102. Chalfie, M., Hart, A. C., Rankin, C. H. & Goodman, M. B. Assaying mechanosensation. *WormBook* https://doi.org/10.1895/wormbook.1.172.1 (2014).

103. Jumper, J. et al. Highly accurate protein structure prediction with AlphaFold. *Nature* **596**, 583–589 (2021).

104. Varadi, M. et al. AlphaFold protein structure database: massively expanding the structural coverage of protein-sequence space with high-accuracy models. *Nucleic Acids Res* **50**, D439–D444 (2022).

Acknowledgements

Author contributions

A.D., F.K.R., L.L., M.W., R.M., E.K., and K.S. performed experiments. A.D., F.K.R., L.L., M.W., R.M., E.K., H.L., S.C., E.J.C., and M.A.H. were involved in interpreting the data and reviewing and editing the paper. A.D. and M.A.H. designed the study and wrote the paper.

Competing interests

The authors declare no competing interests.

Additional information

Supplementary information The online version contains supplementary material available at https://doi.org/10.1038/s41467-024-55105-0.

Correspondence and requests for materials should be addressed to Massimo A. Hilliard.

Peer review information *Nature Communications* thanks Spencer Gibson and the other, anonymous, reviewer(s) for their contribution to the peer review of this work. A peer review file is available.

Reprints and permissions information is available at http://www.nature.com/reprints

Publisher's note Springer Nature remains neutral with regard to jurisdictional claims in published maps and institutional affiliations.